Electronic Supplementary Material

Organic Microporous Crystals Driven by Pure C-H⋯π Interactions with Vapors-Induced Crystal-to-Crystal Transformations

Yu Tian,[a] Jie Yang,[a] Mingxue Gao,[a] Zhenjiang Liu,[a] Meiting Zhao,[a] Manman Fang*[a] and Zhen Li*[abc]

[a]Institute of Molecular Aggregation Science, Tianjin University, Tianjin 300072, China
[b]Department of Chemistry, Wuhan University, Wuhan 430072, China
[c]Joint School of National University of Singapore and Tianjin University, International Campus of Tianjin University, Binhai New City, Fuzhou 350207, China
*Correspondence: manmanfang@tju.edu.cn, lizhen@whu.edu.cn or lizhentju@tju.edu.cn
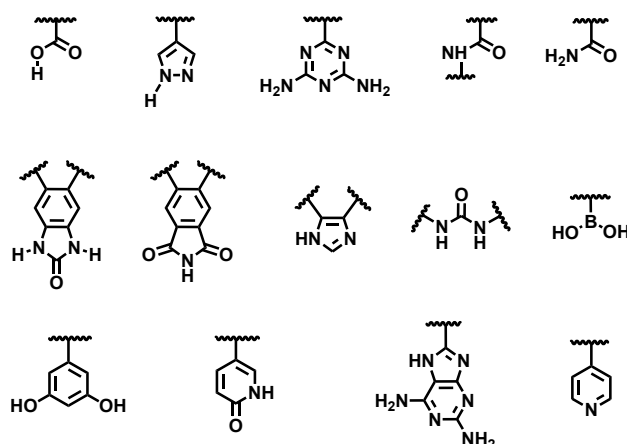
Table of Contents

Chart S1. Various O/N containing organic groups for potential H-bonding units, including carboxylic acid,[S1-S5] pyrazole, [S6] 2,4-diaminotriazine, [S7-S10] amide,[S11] benzimidazolone,[S12] and so on.[S13-S17]

1. Supplemental Experimental Procedures

General Procedures and Materials. All starting chemicals were obtained from commercial sources and used without further purification. Column chromatography was carried out on silica gel using 200-300 mesh. Analytical thin-layer chromatography (TLC) was performed using precoated TLC plates with silica gel GF-254. NMR spectra were obtained with a Bruker spectrometer (^{1}H, ^{13}C, Bruker AVANCE 400 MHz or Bruker AVANCE 600 MHz) using chloroform-*d* (CDCl$_3$) as solvent. The chemical shift references were as follows: (^{1}H) chloroform-*d*, 7.26 ppm, (^{13}C) chloroform-*d*, 77.16 ppm. UV-vis spectra were performed on a Shimadzu UV-2600. Photoluminescence spectra at room temperature and 77 K were performed on a Hitachi F-4700 fluorescence spectrophotometer. Fluorescence decays were obtained using a FLS1000 spectrometer. The powder X-ray diffraction patterns were recorded by RIGAKU MiniFlex600 with an X-ray source of Cu Kα (λ = 1.5418 Å) at 298 K at 40 KV and 15 mA at a scan rate of 7° (2θ)/min (scan range: 5-50°). X-ray single crystal diffractions for compounds were performed on a diffractometer with CCD detector using Cu Kα radiation (λ= 1.5418 Å) source. Melting points were recorder on WRS-2C melting point meter.

Theoretical calculation. The Gaussian 09 program was utilized to perform TD-DFT calculations. The ground state (S$_0$) geometries were obtained from the single crystal structure and no further geometry optimization was conducted in order to maintain the specific molecular configurations and corresponding intermolecular locations. The S$_0$ to S$_1$ vertical transitions were conducted using TD-b3lyp/6-31G*.

Synthesis of compound PBO.

PBO
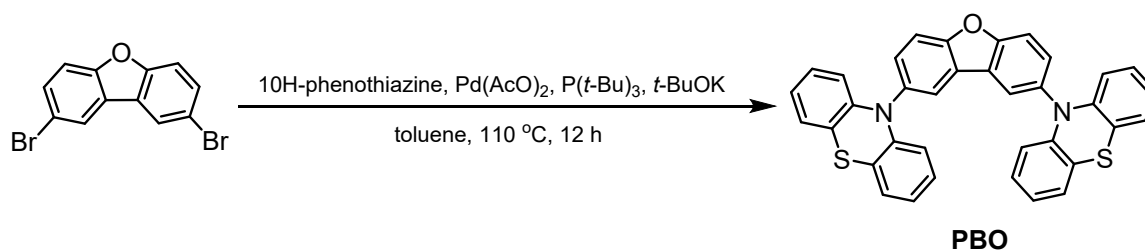
A mixture of phenothiazine (1.99 g, 10 mmol), 2,8-dibromodibenzo[b,d]furan (1.63 g, 5 mmol), potassium tert-butoxide (1.34 g, 12 mmol), palladium acetate (0.11 g, 0.5 mmol) and tri-butylphosphine toluene solution (0.5 mL, 0.25 mmol) were dissolved in toluene (50 mL) in a Schlenk tube and then stirred under N_2 atmosphere and refluxed for 12 h. The solution was concentrated under reduced pressure. The crude product was extracted with dichloromethane and water and dried over anhydrous Na_2SO_4. After removing the solvent, the residue was purified by silica gel column chromatography (petroleum ether/dichloromethane = 5:1) to afford **PBO** as a light white solid (2.56 g, 91%). M.p. 280-282 °C. ^{1}H NMR (400 MHz, CDCl$_3$) δ 7.99 (d, J = 2.0 Hz, 1H), 7.86 (d, J = 8.7 Hz, 1H), 7.55 (dd, J = 8.7, 2.1 Hz, 1H), 7.08-6.99 (m, 2H), 6.93-6.72 (m, 4H), 6.26-6.14 (m, 2H). ^{13}C NMR (100 MHz, CDCl$_3$) δ 156.16, 144.61, 136.32, 131.16, 126.97, 126.27, 123.98, 122.69, 120.26, 116.01, 114.30. HRMS (ESI) m/z calcd for C$_{36}$H$_{22}$N$_2$OS$_2$ (M) 562.1200, found 562.1173.

Synthesis of compound PBS.

PBS
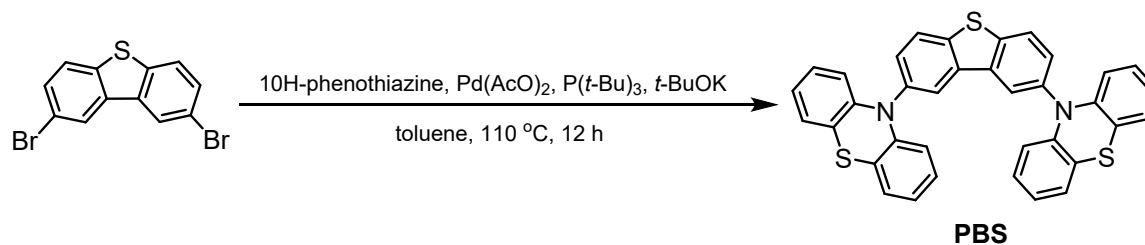
The synthesis of **PBS** is similar to that of **PBO**. A mixture of phenothiazine (1.99 g, 10 mmol), 2,8-dibromodibenzo[b,d]thiophene (1.71 g, 5 mmol), potassium tert-butoxide (1.34 g, 12 mmol), palladium acetate (0.11 g, 0.5 mmol) and tri-butylphosphine toluene solution (0.5 mL, 0.25 mmol) were dissolved in toluene (50 mL) in a Schlenk tube and then stirred under N_2 atmosphere and refluxed for 12 h. The solution was concentrated under reduced pressure. The crude product was extracted with dichloromethane and water and dried over anhydrous Na_2SO_4. When removed the solvent, the residue was purified by silica gel column chromatography (petroleum ether/dichloromethane = 5:1) to afford **PBS** as a white solid (2.51 g, 87%). M.p. 306-308 °C. ^{1}H NMR (400 MHz, CDCl$_3$) δ 8.17 (d, J = 1.9

Hz, 1H), 8.12 (d, J = 8.4 Hz, 1H), 7.54 (dd, J = 8.4, 2.0 Hz, 1H), 7.07-6.99 (m, 2H), 6.82 (dd, J = 6.8, 2.9 Hz, 4H), 6.25 (dd, J = 7.4, 2.0 Hz, 2H). ^{13}C NMR (100 MHz, CDCl$_3$) δ 144.42, 139.86, 138.35, 137.68, 130.24, 127.00, 126.96, 125.23, 124.43, 122.79, 120.66, 116.32. HRMS (ESI) m/z calcd for C$_{36}$H$_{22}$N$_2$S$_3$ (M) 578.0945, found 578.0944.

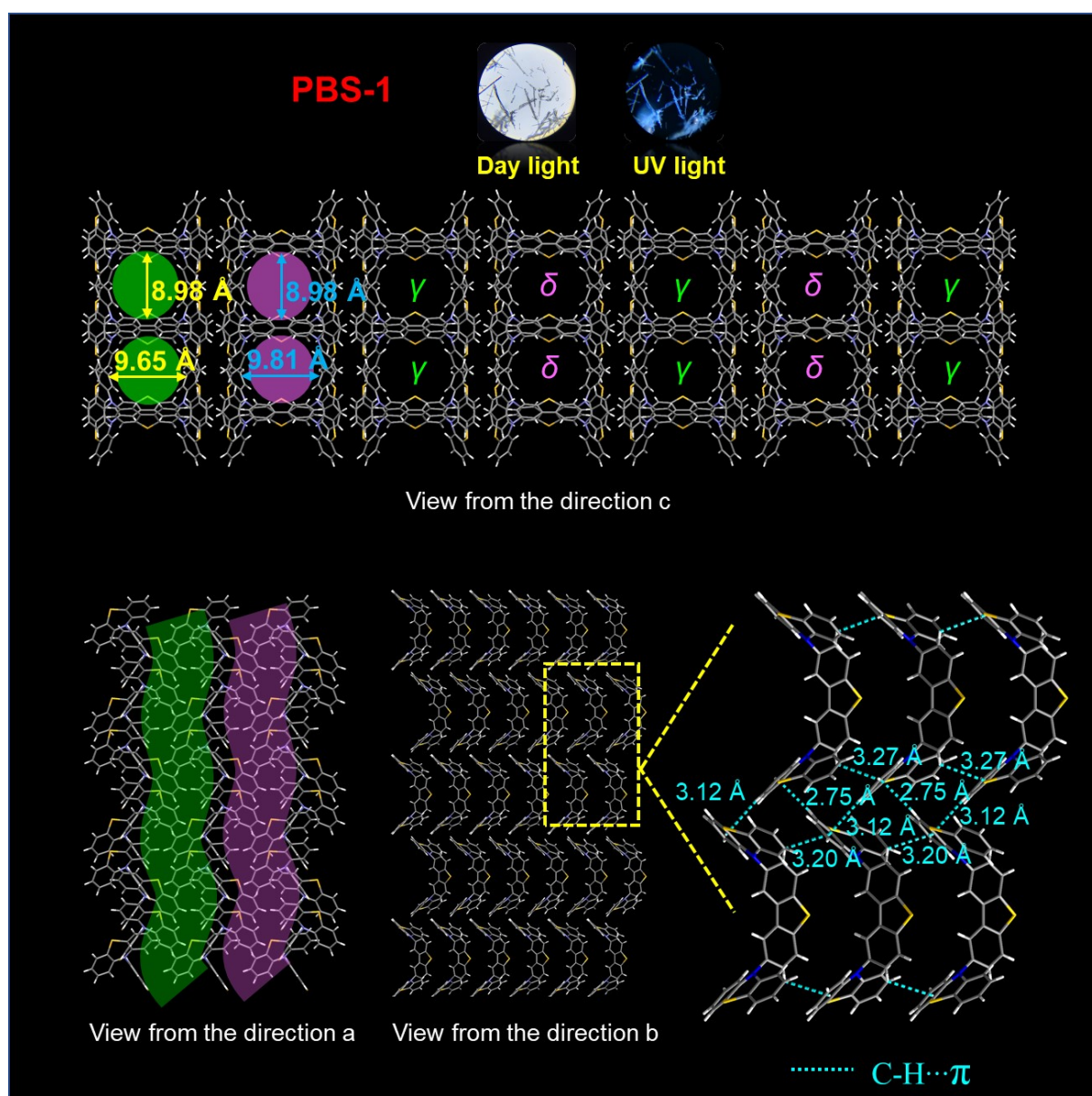## 2. Crystal Structures, data and theoretical calculation (Figures S1-S5)

Figure S1. Molecular packing of **PBS-1** crystal observed from a, b, and c directions, respectively, including channel size analyses and molecular interactions, the blue dotted lines are C-H···π interactions.
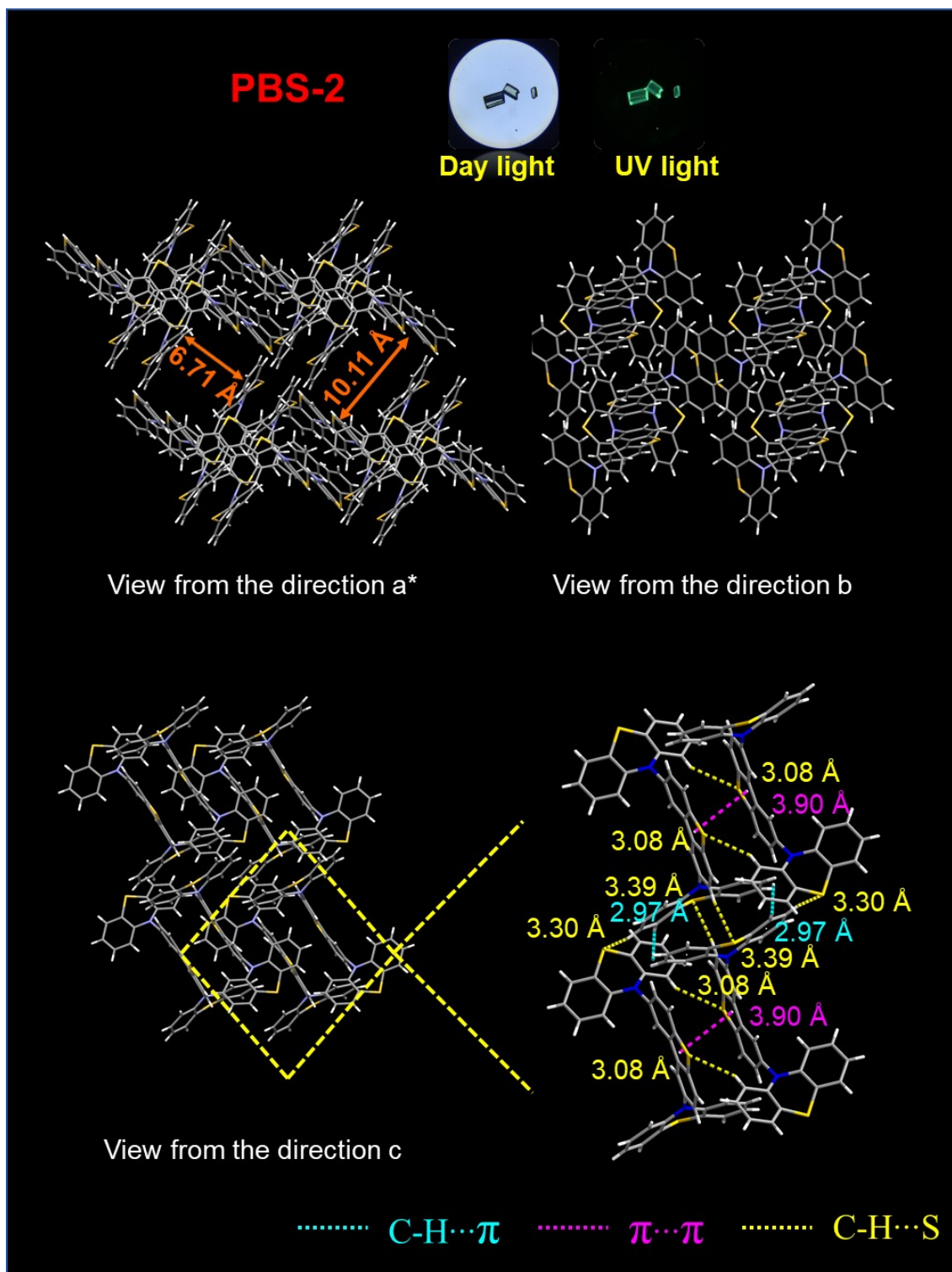
Figure S2. Molecular packing of **PBS-2** crystal observed from a, b, and c directions, respectively, including channel size analyses and molecular interactions, the blue dotted lines are C-H···π interactions, the pink dotted line is the π···π interactions and the yellow dotted line is the C-H···S interactions.

Table S1. Crystals data and structure refinement for **PBO-1**, **PBO-2**, **PBO-3**, **PBS-1** and **PBS-2**.

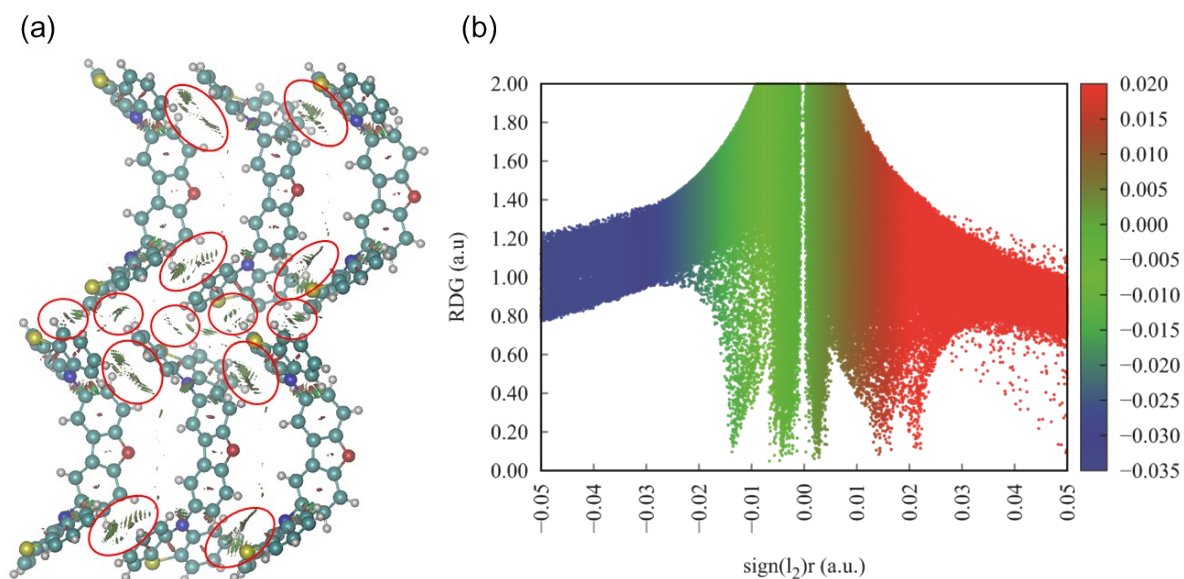| Compound	PBO-1	PBO-2	PBO-3	PBS-1	PBS-2
Formula	$C_{36}H_{22}N_2OS_2$	$2(C_{36}H_{22}N_2OS_2)$, CCl_2	$C_{36}H_{22}N_2OS_2$, $1(C_7H_8)$	$C_{36}H_{22}N_2S_3$	$2(C_{36}H_{22}N_2S_3)$, CCl_2
M_w	562.68	1210.28	654.81	578.73	1242.40
Temp (K)	293	293	293	293	293
Crystal system	orthorhombic	monoclinic	monoclinic	orthorhombic	triclinic
Space group	Pmc21	P1 21/c 1	C12/c1	Pmc21	P-1
a (Å)	29.9077 (2)	14.3600 (2)	28.6573 (6)	28.6595 (5)	8.8209 (2)
b (Å)	9.2309 (1)	14.8334 (2)	6.7631 (1)	8.9864 (2)	13.8123 (3)
c (Å)	12.7695 (1)	14.0298 (1)	36.8149 (7)	13.6296 (2)	14.3266 (3)
α (deg)	90.00	90.00	90	90.00	65.894 (2)
β (deg)	90.00	103.79 (1)	107.502 (2)	90.00	72.183 (2)
γ (deg)	90.00	90.00	90	90.00	71.871 (2)
V (Å^3)	3525.35 (5)	2902.30 (6)	6804.9 (2)	3510.24 (11)	1481.64 (6)
Z	4	4	8	4	2
ρ_c (g/cm^3)	1.060	1.396	1.278	1.095	1.380
μ (mm^{-1})	1.570	2.780	1.702	2.109	2.535
F (000)	1168.0	1260.0	2736.0	1200.0	638.0
CCDC	2027490	2027489	2027488	2027487	2124202

(a) (b)

Figure S3. Reduced density gradient isosurface map with isovalue of 0.05 of **PBO-1** crystal, the value of Sign(l_2)r in surfaces is represented by filling color according to the color bar in upper right corner. For clarity, the interactions of C-H···π between neighbor **PBO-1** are marked by the green circle.
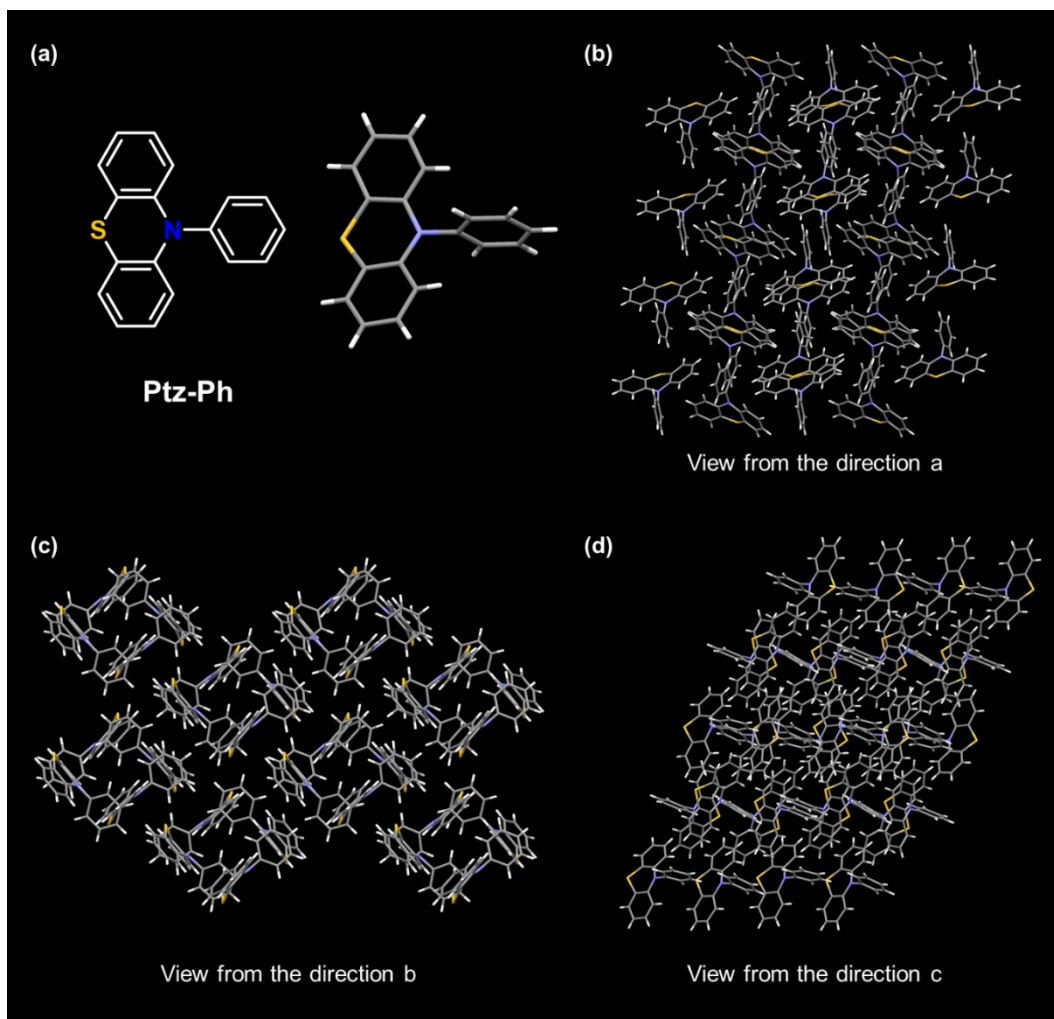
(a) (b)
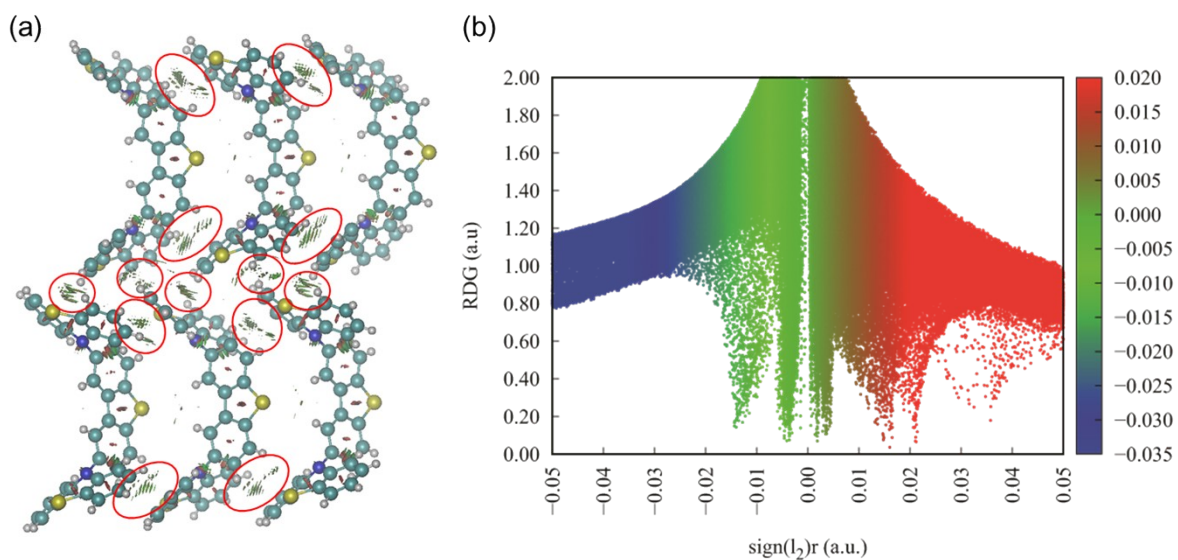
Figure S4. Reduced density gradient isosurface map with isovalue of 0.05 of **PBS-1** crystal, the value of Sign(l_2)r in surfaces is represented by filling color according to the color bar in upper right corner. For clarity, the interactions of C-H···π between neighbor **PBO-1** are marked by the green circle.

Figure S5. Chemical structure and molecular packing of **Ptz-Ph**.

3. Stability and Gas Adsorption (TGA, DSC, PXRD) (Figures S6-S14)
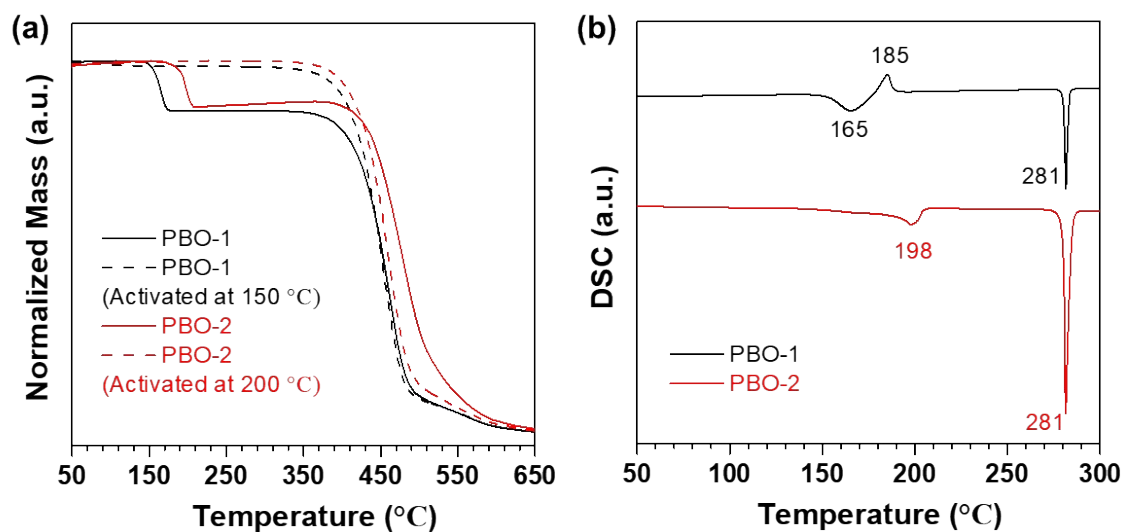
Figure S6. a) The TGA patterns for the crystals of **PBO-1** before and after being activated at 150 °C, and **PBO-2** before and after being activated at 200 °C; b) DSC curves of **PBO-1** and **PBO-2**.
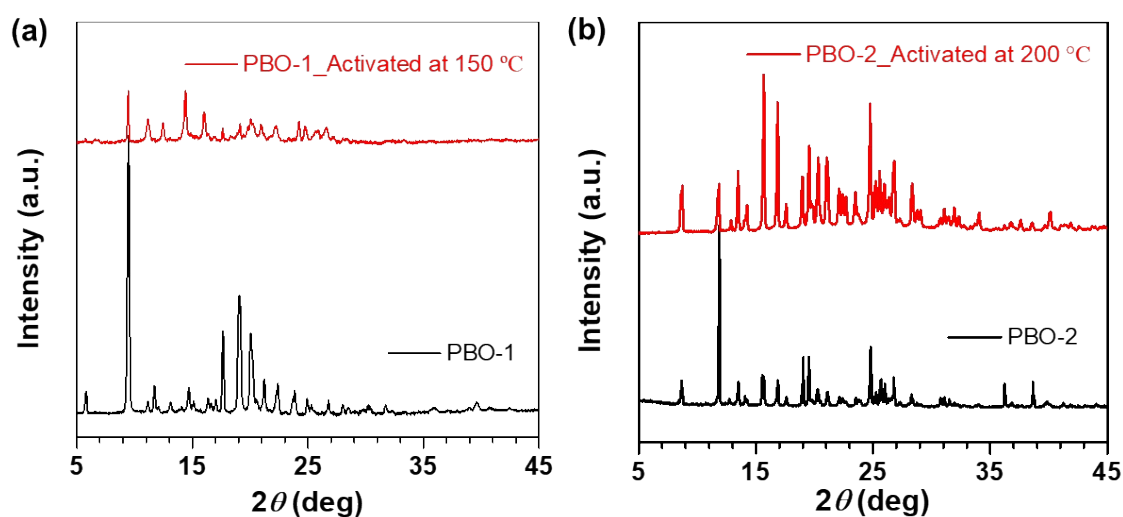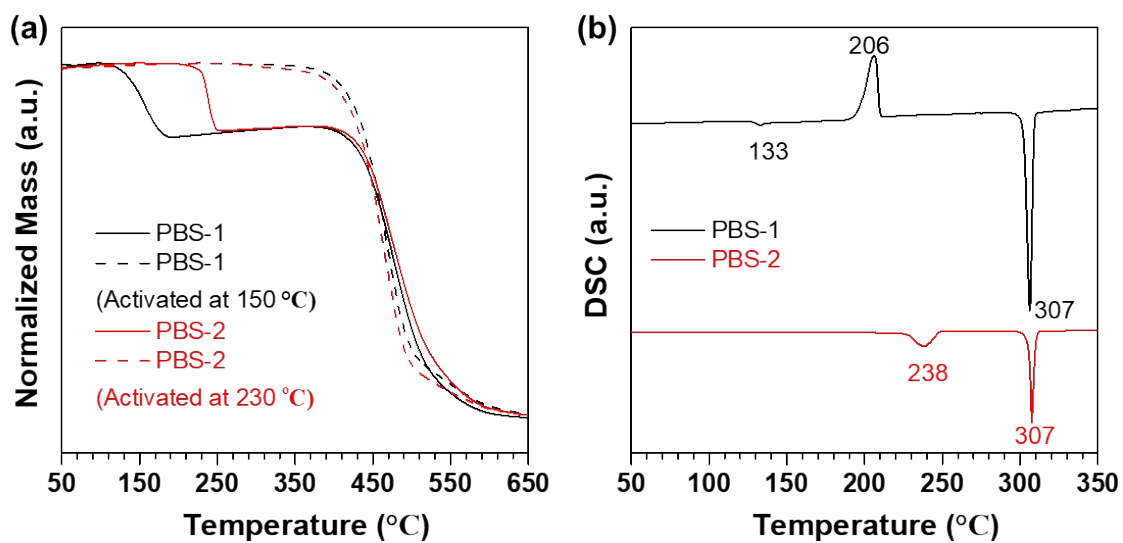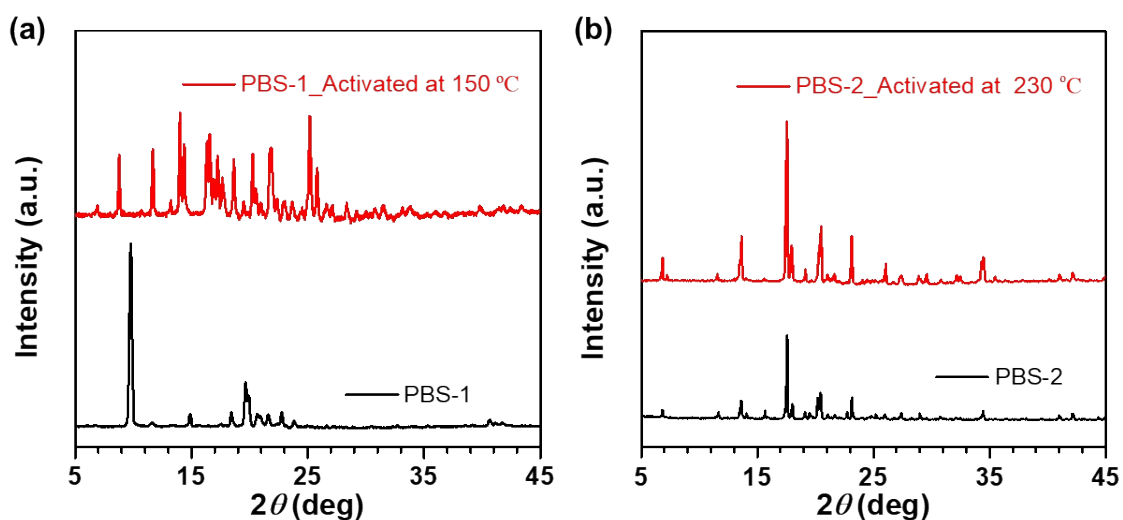

Figure S7. a) The PXRD patterns for the powders of **PBO-1** before and after being activated at 150 °C; b) The PXRD patterns for the powders of **PBO-2** before and after being activated at 200 °C.
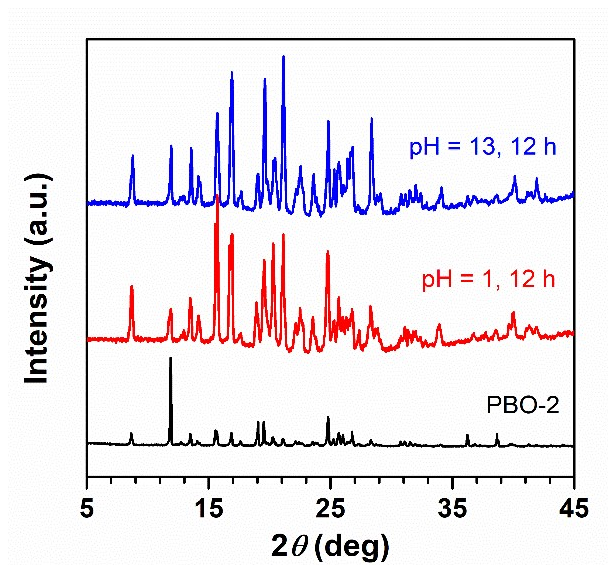
Figure S8. a) The TGA curves for the crystals of **PBS-1** before and after being activated at 150 °C, and **PBS-2** before and after being activated at 230 °C; b) DSC curves of **PBS-1** and **PBS-2**.

Figure S9. a) The PXRD patterns for the powders of **PBS-1** before and after being activated at 150 °C; b) The PXRD patterns for the powders of **PBS-2** before and after being activated at 230 °C.

Figure S10. PXRD patterns of **PBO-2** after being treated with different pH aqueous solutions.
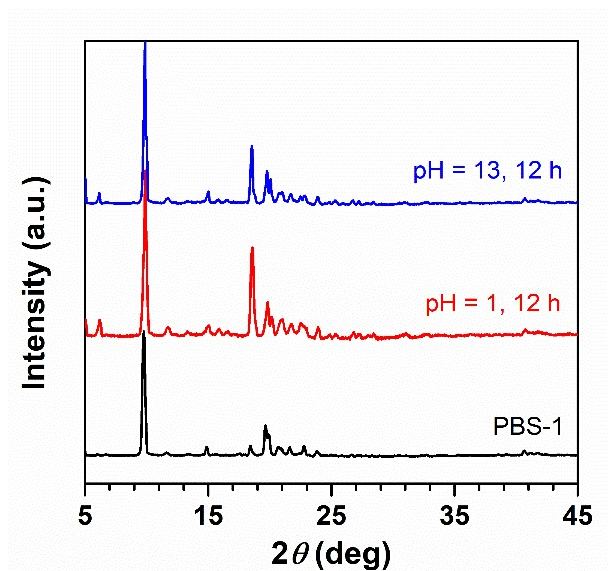
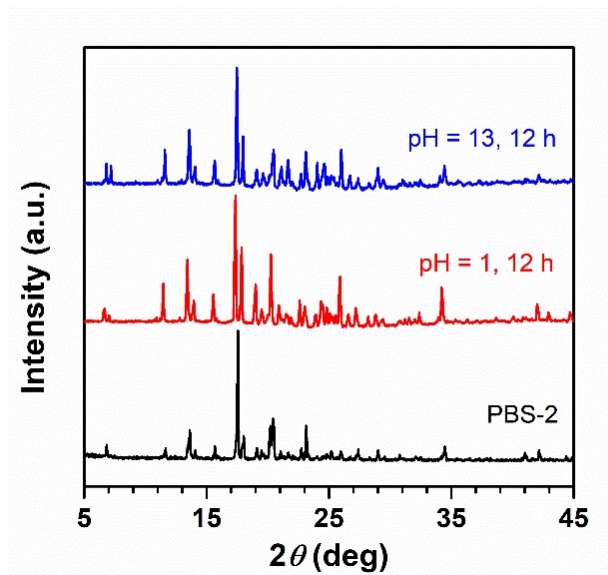**Figure S11.** PXRD patterns of **PBS-1** after being treated with different pH aqueous solutions.

Figure S12. PXRD patterns of **PBS-2** after being treated with different pH aqueous solution.
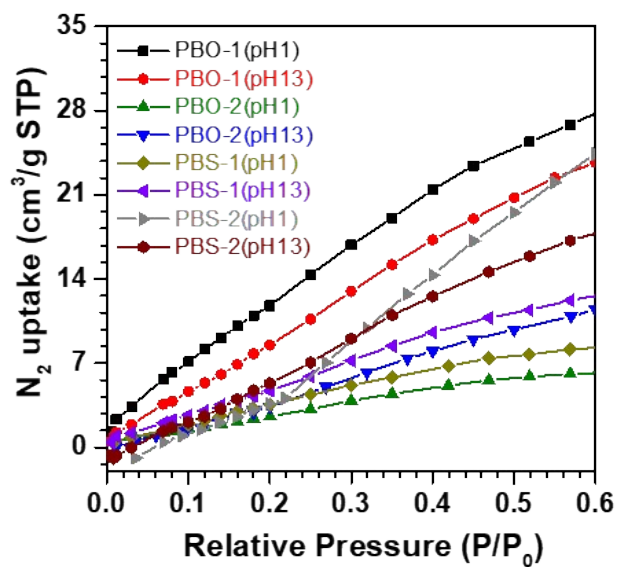

Figure S13. N_2 adsorption isotherms of **PBO-1**, **PBO-2**, **PBS-1** and **PBS-2** treated with different pH aqueous for 12 h. (77 K)
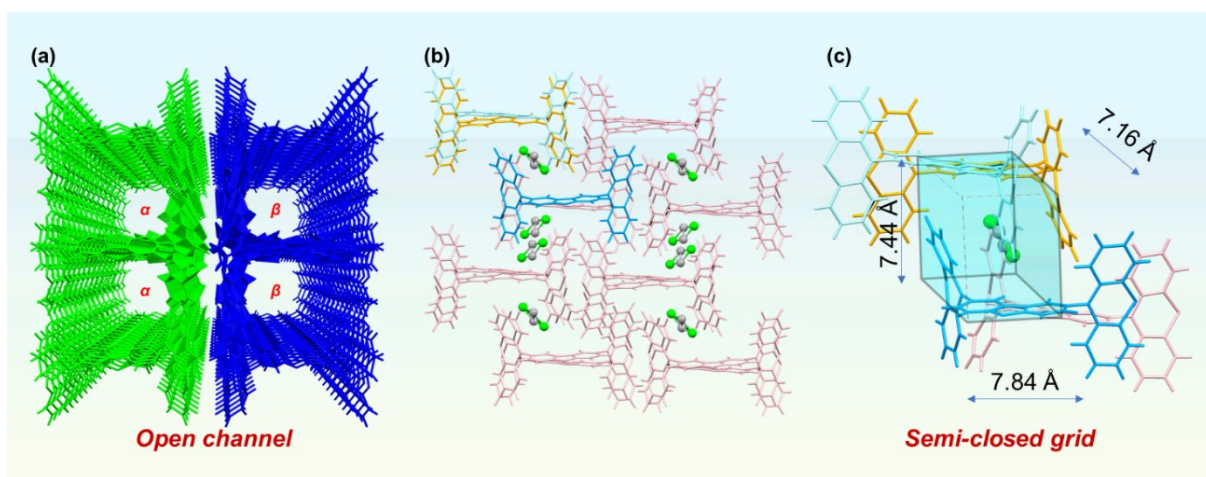
Figure S14. PBO-1 channels display (a) and **PBO-2** semi-closed grid display (Contains solvent molecules) (b and c).

About the theoretical calculation of BET

The simulation methods for BET surface area and pore size distribution are based on the Voronoi decomposition according the algorithm implemented with free software, Zeo++.

Zeo++'s core functions: T.F. Willems, C.H. Rycroft, M. Kazi, J.C. Meza, and M. Haranczyk, Algorithms and tools for high-throughput geometry-based analysis of crystalline porous materials, Microporous and Mesoporous Materials, 149 (2012) 134-141, DOI: 10.1016/j.micromeso.2011.08.020.

Pore size distributions and stochastic ray tracing: M. Pinheiro, R.L. Martin, C.H. Rycroft, A. Jones, E. Iglesia, and M. Haranczyk, Characterization and comparison of pore landscapes in crystalline porous materials, Journal of Molecular Graphics and Modeling 44 (2013) 208-219 DOI: 10.1016/j.jmgm.2013.05.007.

Data Summary (N_2 with a kinetic radius of 1.86 Å was used as the probe molecule, so that the pore with size smaller than N_2 could not be probed).

The theoretical calculation results are as follows and 'desol' means that solvent molecules are subjectively removed:

Table S2. Theoretical BET values of **PBO-1**, **PBO-2**, **PBS-1** and **PBS-2**.

Name	BET (Theoretical value) (m^2/g)
PBO-1	726.026
PBO-2	0
PBO-2-desol	63.679
PBS-1	616.862
PBS-2	0
PBS-2-desol	96.475

4. Photophysical Properties and Theoretical Calculation (Figures S15-S22)
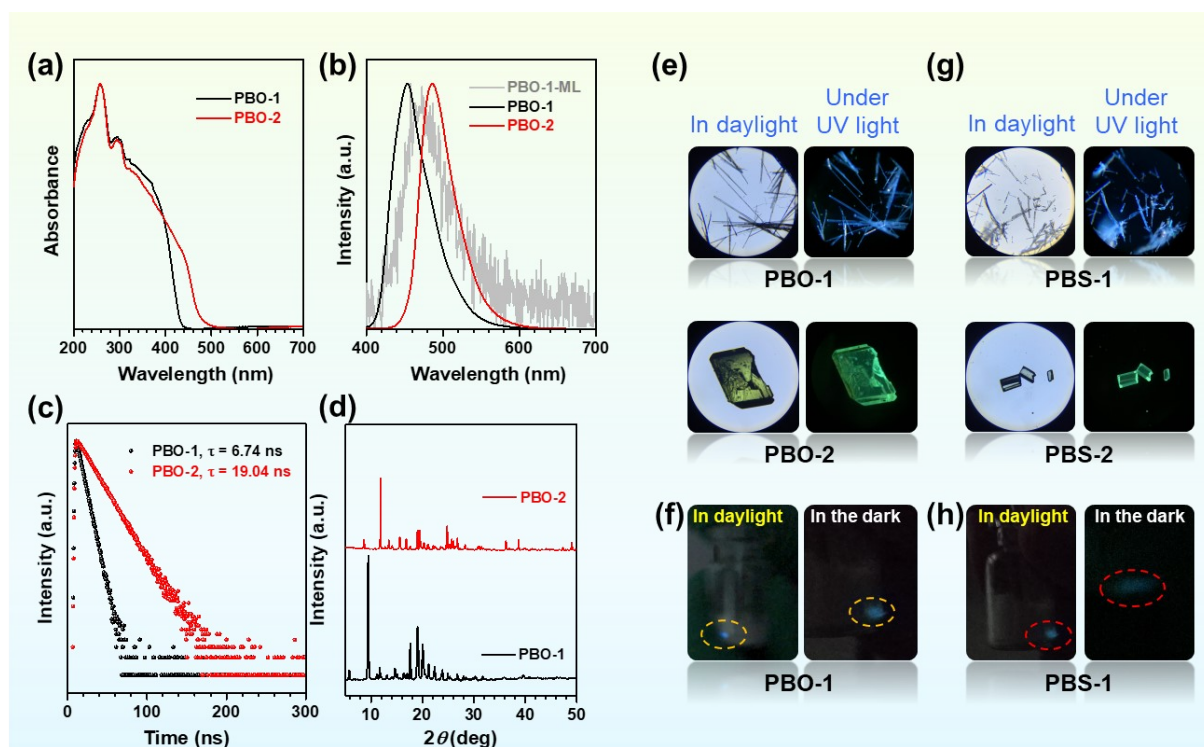
Figure S15. The normalized UV-visible spectra (a), PL spectra and ML spectrum (b), fluorescence decay curves (c) and PXRD patterns (d) for the powders of crystal **PBO-1** and crystal **PBO-2**. Photographs of crystals **PBO-1** and crystal **PBO-2** (e), **PBS-1** and crystal **PBS-2** (g) under natural light and 365 nm ultraviolet light. ML Photographs of crystals **PBO-1** (f) and **PBS-1** (h).

Table S3.   Optical data of crystals, space group and ML information.

Compound	Solution	λ_{em} / nm	τ_{PL} / ns	Φ_{PL} / %	Crystal system	Space group	ML
PBO-1	CH_2Cl_2/PE	454	6.74	1.05	orthorhombic	$Pmc2_1$ (***non-centrosymmetric***)	active
PBO-2	CH_2Cl_2	487	19.04	4.78	monoclinic	$P121/c\ 1$ (***centrosymmetric***)	inactive
PBS-1	CH_2Cl_2/PE	451	6.23	2.11	orthorhombic	$Pmc2_1$ (***non-centrosymmetric***)	active
PBS-2	CH_2Cl_2	487	12.22	3.64	triclinic	$P\text{-}1$ (***centrosymmetric***)	inactive

16

In order to make clearer displays of mechanoluminescence phenomena, the mechanoluminescence
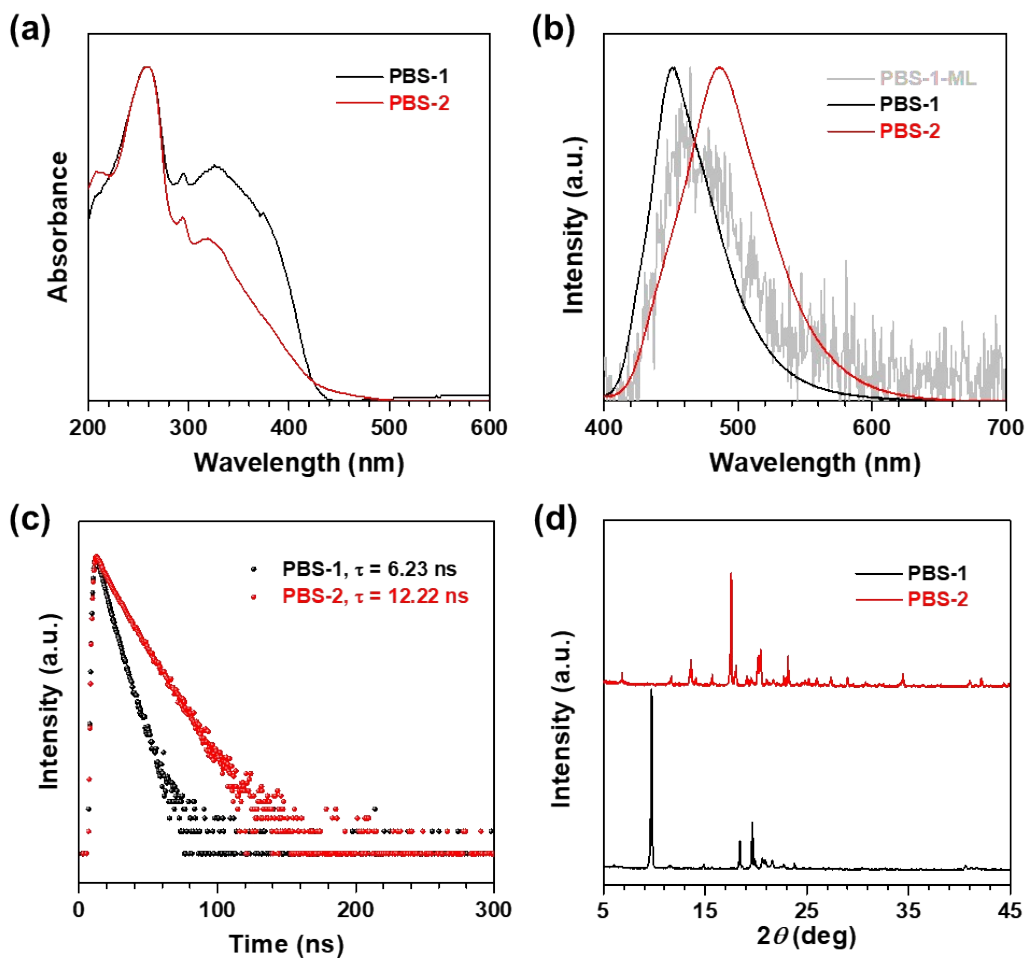panoramic photos were prov

Figure S17. ML Photograph of
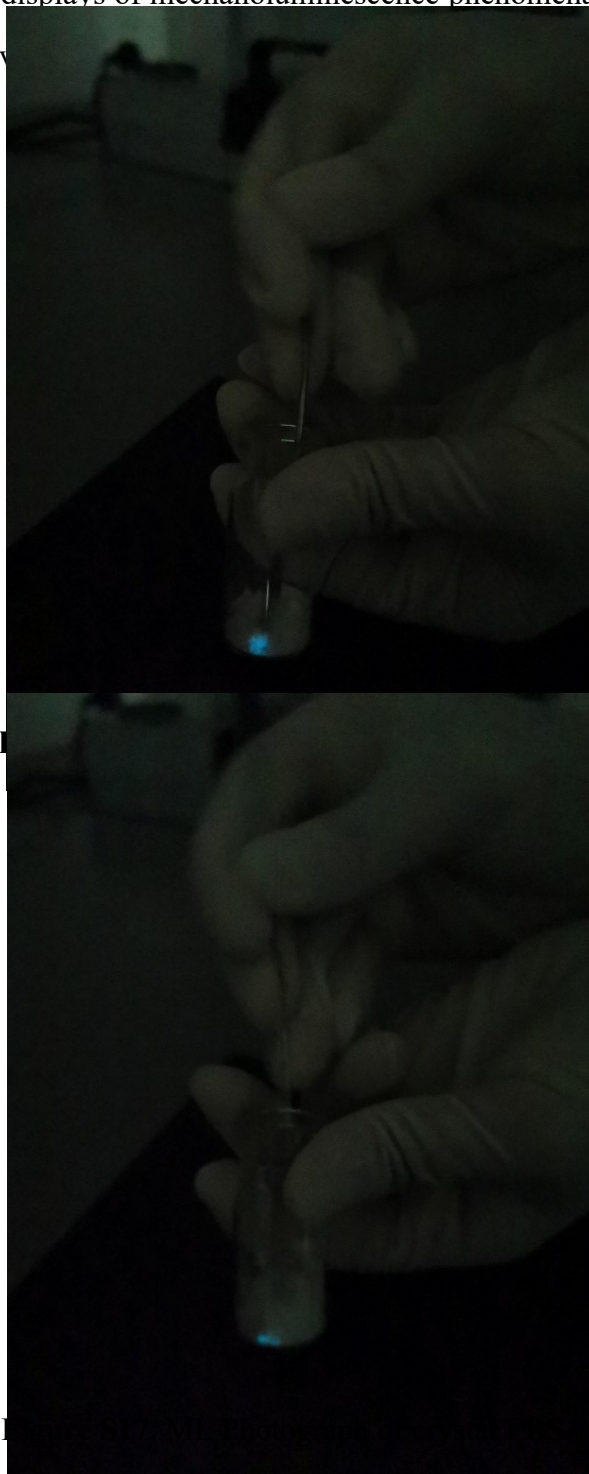
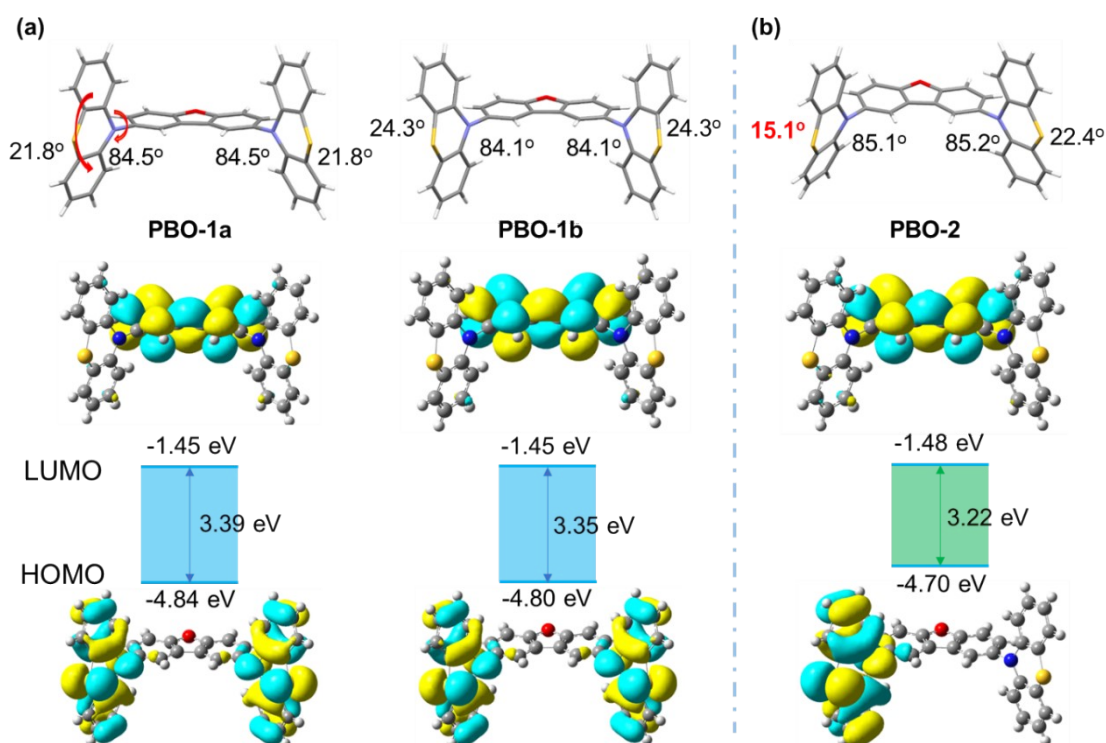**Figure S18.** (a) The normalized UV-visible spectra of crystal **PBS-1** and crystal **PBS-2** at room temperature. (b) The PL spectra of crystal **PBS-1** and crystal **PBS-2**, and ML spectrum of **PBS-1** at room temperature. (c) Fluorescence decay curves of crystal **PBS-1** and crystal **PBS-2** at room temperature. (d) The PXRD patterns for the powders of crystal **PBS-1** and crystal **PBS-2**.

Figure S19. (a) Single molecule in crystal **PBO-1** and their HOMO, LUMO orbitals, where **PBO-1a** and **PBO-1b** are two different molecular conformations in crystal **PBO-1**. (b) Single molecule in crystal **PBO-2** and their HOMO, LUMO orbitals.

For crystal **PBO-1**, two different molecular conformations of **PBO-1a** and **PBO-1b** can be observed, and they are all symmetrical (Fig. S19a). The dihedral angles of the two benzene rings in phenothiazine both are 21.8°, and the twist angles between phenothiazine and dibenzofuran both are 84.5° in crystal **PBO-1a**. Similarly, the dihedral angles both are 24.3° and the twist angles both are 84.1° in crystal **PBO-1b** (Fig. S19a). However, in crystal **PBO-2**, only one asymmetric molecular conformation could be observed that the dihedral angles of the two benzene rings in phenothiazine are 15.1° and 22.4°, and the twist angles between phenothiazine and dibenzofuran are 85.1° and 85.2° respectively (Fig. S19b). Therefore, the more planar phenothiazine units in crystal **PBO-2** may be responsible for the more red-shifted absorption and emission. In addition, obviously intramolecular charge transfer (CT) transition can be found for **PBO-1a**, **PBO-1b** and **PBO-2** as indicated time-dependent density functional theory (TD-DFT) calculations results, and the band gaps of **PBO-1a** and **PBO-1b** are 3.39 eV and 3.35 eV respectively, which are larger than 3.22 eV of **PBO-2**.
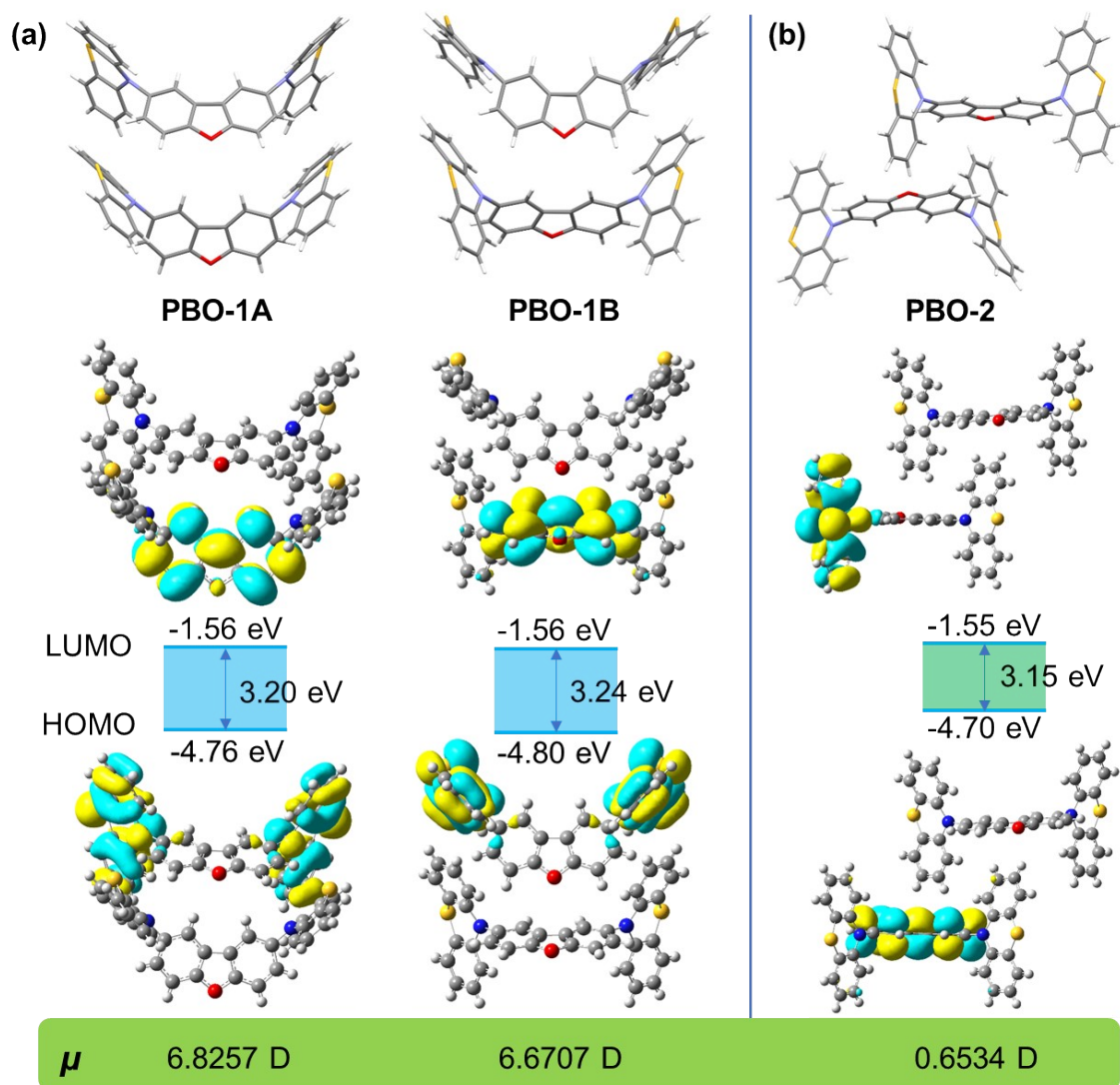
Figure S20. Dimers in crystal **PBO-1** and their HOMO, LUMO orbitals, where **PBO-1A** and **PBO-1B** are two different dimers in crystal **PBO-1**. (b) Dimer in crystal **PBO-2** and their HOMO, LUMO orbitals.

Their respective dimers also undergo intermolecular charge transfer transitions (Fig. S20), the energy band gaps of **PBO-1A** and **PBO-1B** are 3.20 eV and 3.24 eV, respectively, but **PBO-2** is only 2.96 eV. These results could further explain that the absorbance and emission of crystal **PBO-2** are red-shifted than that of crystal **PBO-1**, confirming the important influence of molecular conformation and molecular packing on photophysical properties again.
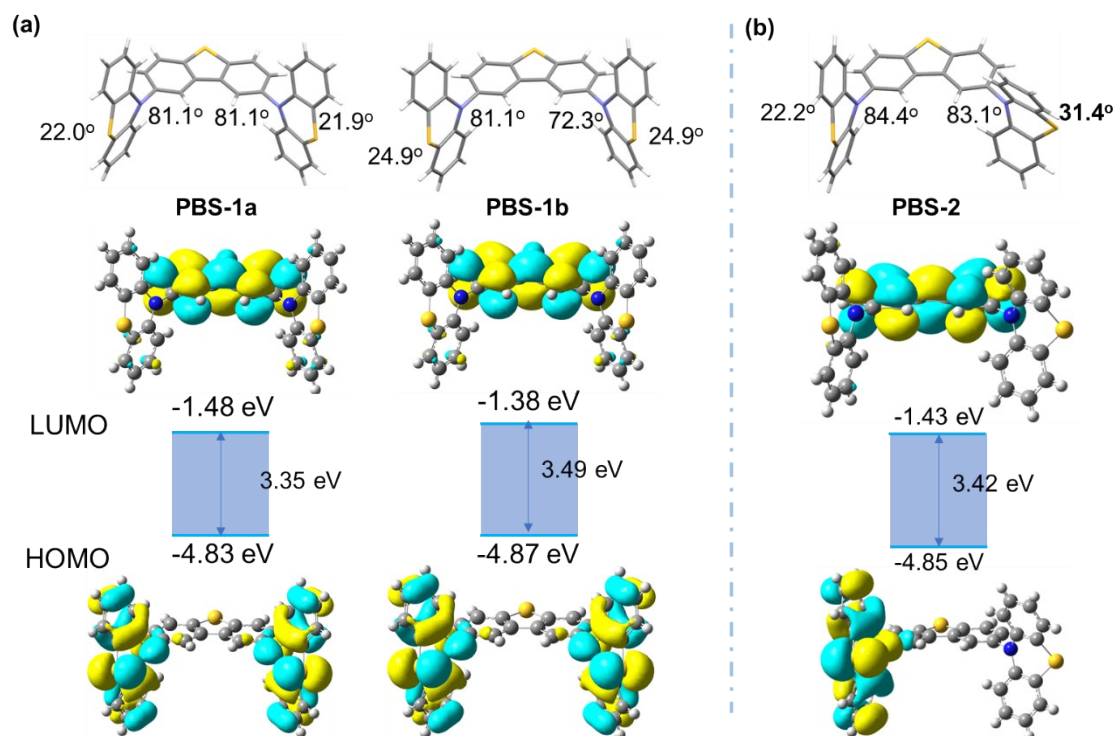
Figure S21. Single crystal structure analyses, HOMO, LUMO orbitals and band gaps of **PBS-1** and **PBS-2**. Dihedral angles between two benzene rings in phenothiazine are 22.0° and 21.9° respectively in **PBS-1a**, and the twist angles between phenothiazine and dibenzothiophene both are 81.1° in **PBS-1a.** Dihedral angles between two benzene rings in phenothiazine both are 24.9° in **PBS-1b**, and the twist angles between phenothiazine and dibenzothiophene are 81.1° and 72.3° respectively in **PBS-1b**. **PBS-1a** and **PBS-1b** are two different molecular conformations in crystal **PBS-1**. Dihedral angles between two benzene rings in phenothiazine are 22.2° and 31.4° respectively in **PBS-2**, and the twist angles between phenothiazine and dibenzothiophene are 84.4° and 83.1° respectively in **PBS-2.**

(a)

(b)

	PBS-1A	PBS-1A	PBS-2
LUMO	-1.57 eV	-1.48 eV	-1.47 eV
	3.18 eV	3.31 eV	3.44 eV
HOMO	-4.75 eV	-4.79 eV	-4.91 eV

μ	7.0540 D	7.1070 D	0.0002 D
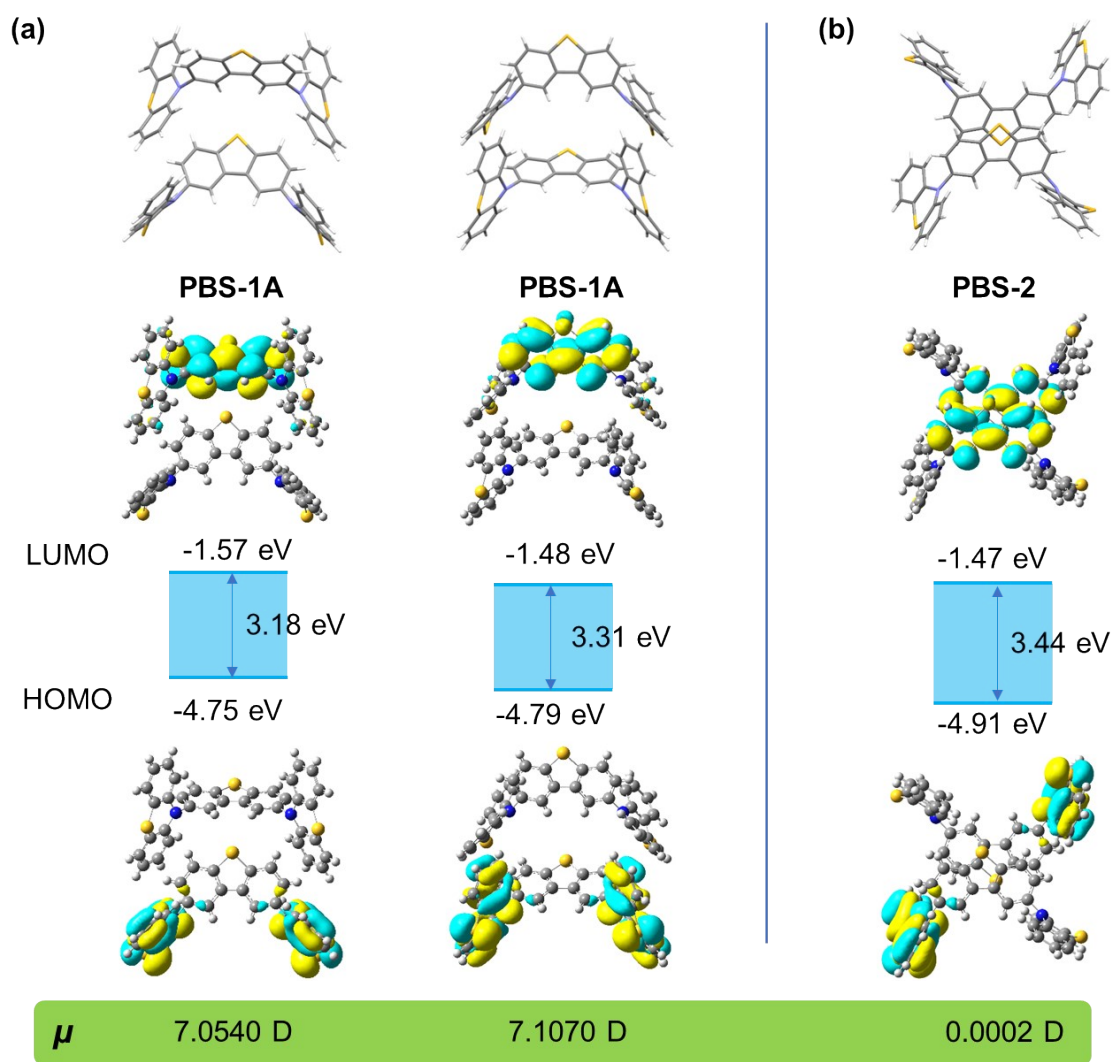
Figure S22. (a) Dimers in crystal **PBS-1** and their HOMO, LUMO orbitals. (b) Dimer in crystal **PBS-2** and their HOMO, LUMO orbitals. **PBS-1A** and **PBS-1B** are two different dimers in crystal **PBS-1**. (μ values are their dipole moments)

# 5. Crystal-to-Crystal Transformations (CCT) Used for Toluene Adsorption and Desorption (Figures S23-S47)
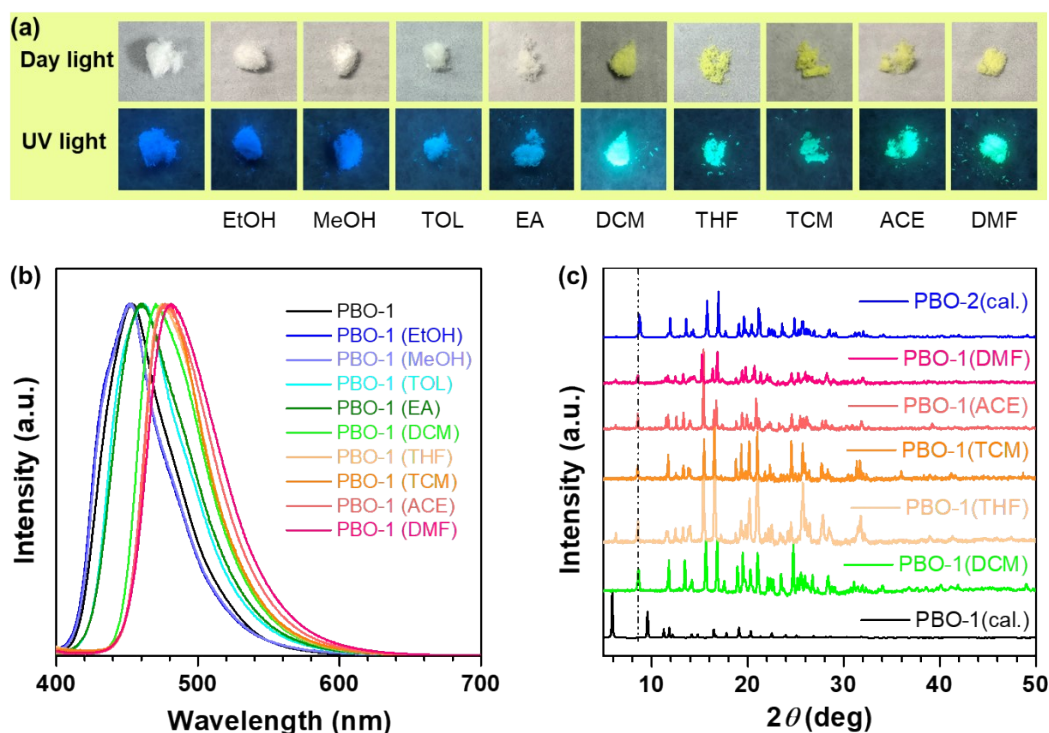
Figure S23. Photographs under day light and ultraviolet lamp (a), photoluminescence spectra (b) and PXRD (c) of crystal **PBO-1** before and after exposure to EtOH, MeOH, TOL, EA, DCM, THF, TCM, ACE and DMF solvents. (cal. is theoretical calculation simulation patterns).
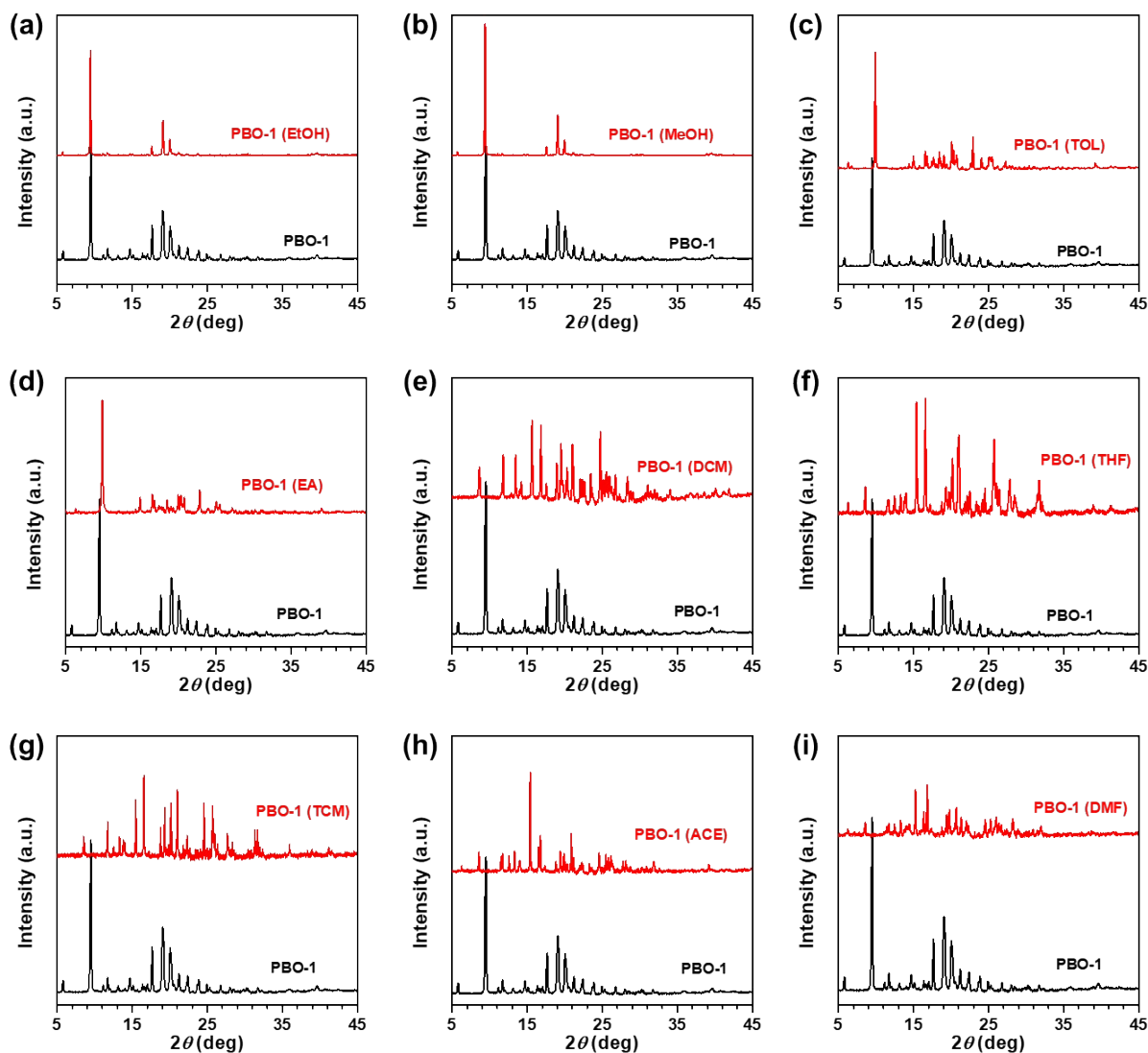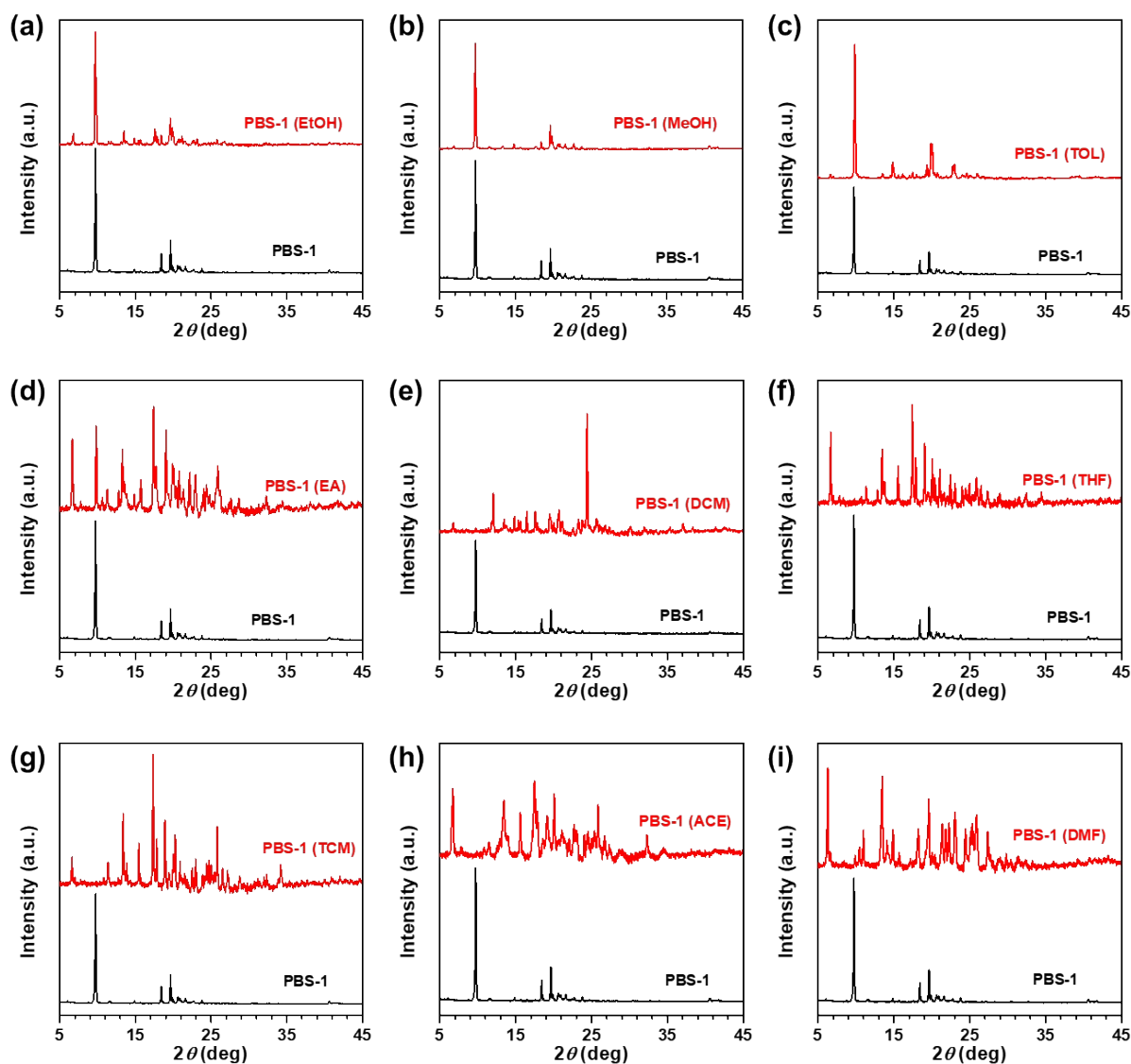
Figure S24. PXRD patterns for the powders of **PBO-1** before and after exposure to different solvent vapors. The black lines are the PXRD patterns for the powders of **PBO-1**, the red lines are the PXRD patterns for the powders of **PBO-1** after exposure to corresponding solvent vapors. Brackets indicate that the solvent vapor has been used.
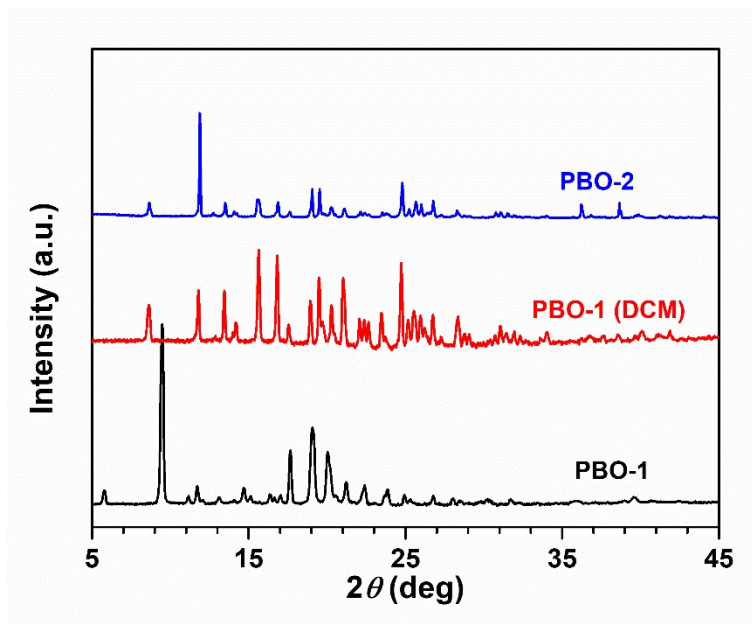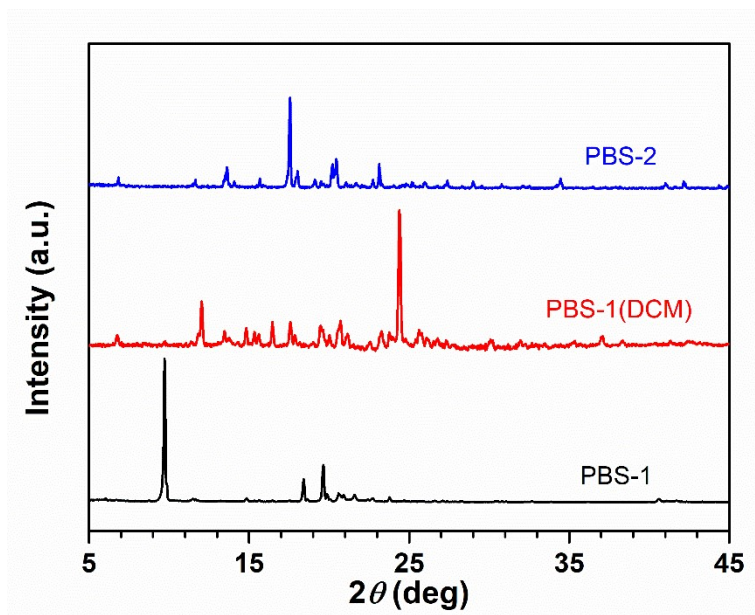
Figure S25. PXRD patterns for the powders of **PBO-1** before and after exposure to DCM vapor. The black line is the PXRD pattern for the powders of **PBO-1**, the red line is the PXRD pattern for the powders of **PBO-1** after exposure to DCM vapor. The blue pattern (PXRD pattern of **PBO-2**) is for comparison.
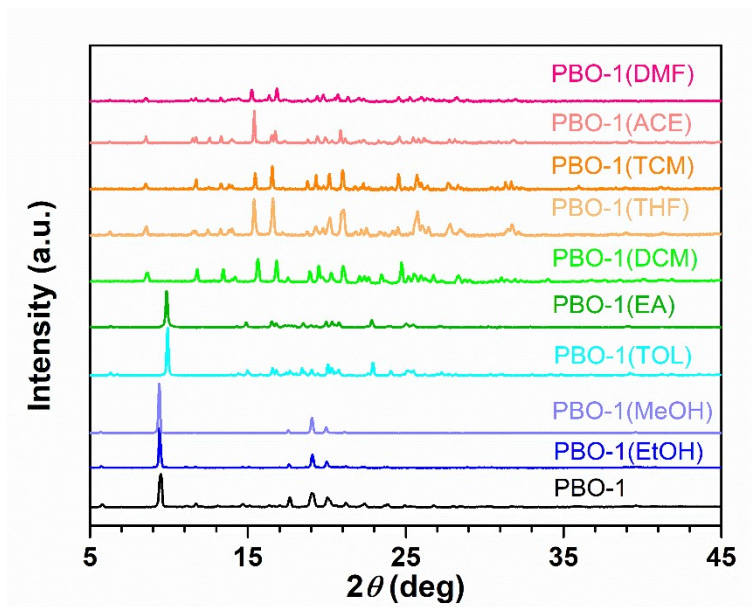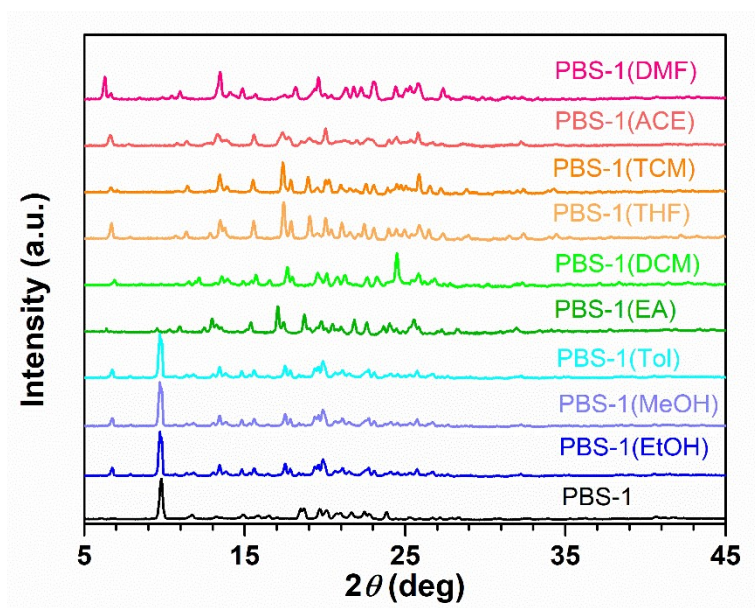

Figure S26. Powder X-ray diffraction patterns of crystal **PBO-1** before and after exposure to EtOH, MeOH, TOL, EA, DCM, THF, TCM, ACE and DMF vapours.
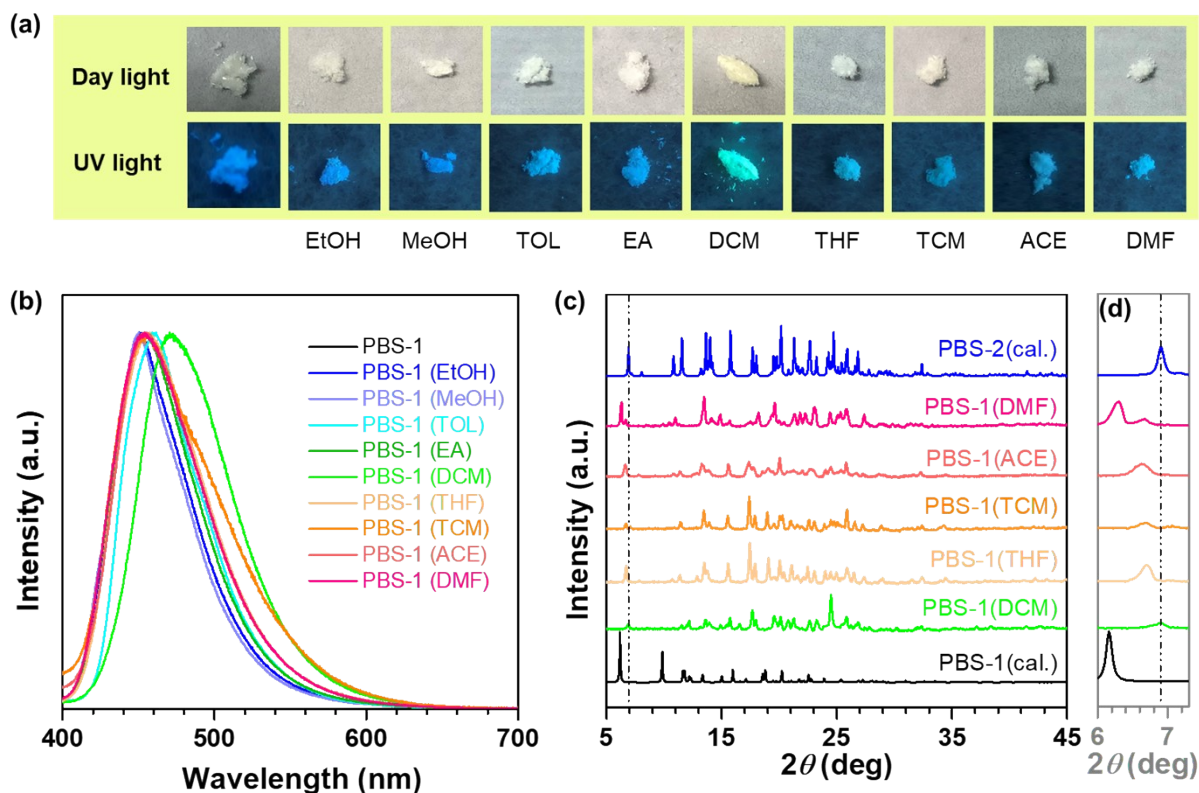
Figure S27. Photographs under day light and ultraviolet lamp (a), photoluminescence spectra (b) and powder X-ray diffraction patterns (c) of crystal **PBS-1** before and after exposure to EtOH, MeOH, TOL, EA, DCM, THF, TCM, ACE and DMF vapours. Figure d is a partial enlarged view of Figure c. (cal. is theoretical calculation simulation patterns)

Figure S28. The PXRD patterns for the powders of **PBS-1** before and after exposure to different solvent vapors. The black lines are the PXRD patterns for the powders of **PBS-1**, the red lines are the PXRD patterns for the powders of **PBS-1** after exposure to corresponding solvent vapor. Brackets indicate that the solvent vapor has been used.

Figure S29. PXRD patterns for the powders of **PBS-1** before and after exposure to DCM vapor. The black line is the PXRD pattern for the powders of **PBS-1**, the red line is the PXRD pattern for the powders of **PBS-1** after exposure to DCM vapor. The blue pattern (PXRD pattern of **PBS-2**) is for comparison.

Figure S30. Powder X-ray diffraction patterns of crystal **PBS-1** before and after exposure to EtOH, MeOH, TOL, EA, DCM, THF, TCM, ACE and DMF vapours.
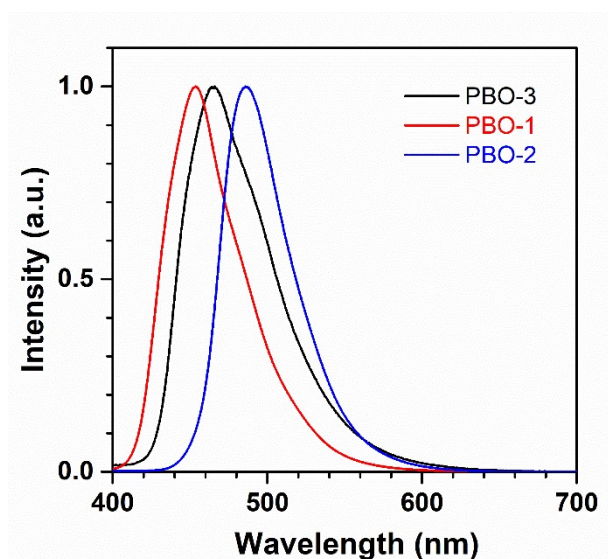
Figure S31. Photoluminescence (PL) spectra of **PBO-1**, **PBO-2** and **PBO-3**. (λ_{ex} = 365 nm)
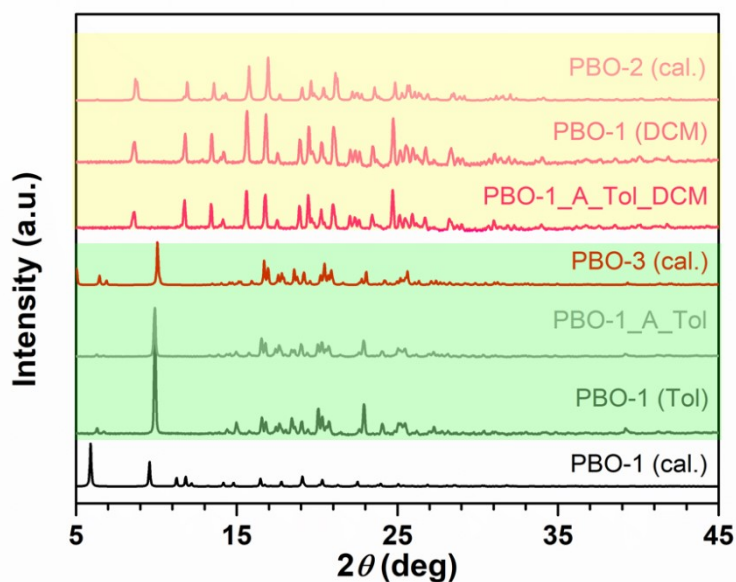
Figure S32. Powder X-ray diffraction patterns of crystal **PBO-1** (cal.) (Pattern simulated with crystal **PBO-1**), **PBO-1** (Tol) (**PBO-1** is exposed to toluene vapour), **PBO-1_A_Tol** (**PBO-1** is exposed to toluene vapour after high temperature activation), **PBO-3** (cal.) (Pattern simulated with crystal **PBO-3**), **PBO-1_A_Tol_DCM** (**PBO-1_A_Tol** is exposed to dichloromethane vapour), **PBO-1** (DCM) (**PBO-1** is exposed to dichloromethane vapour) and **PBO-2** (cal.) (Pattern simulated with crystal **PBO-2**).
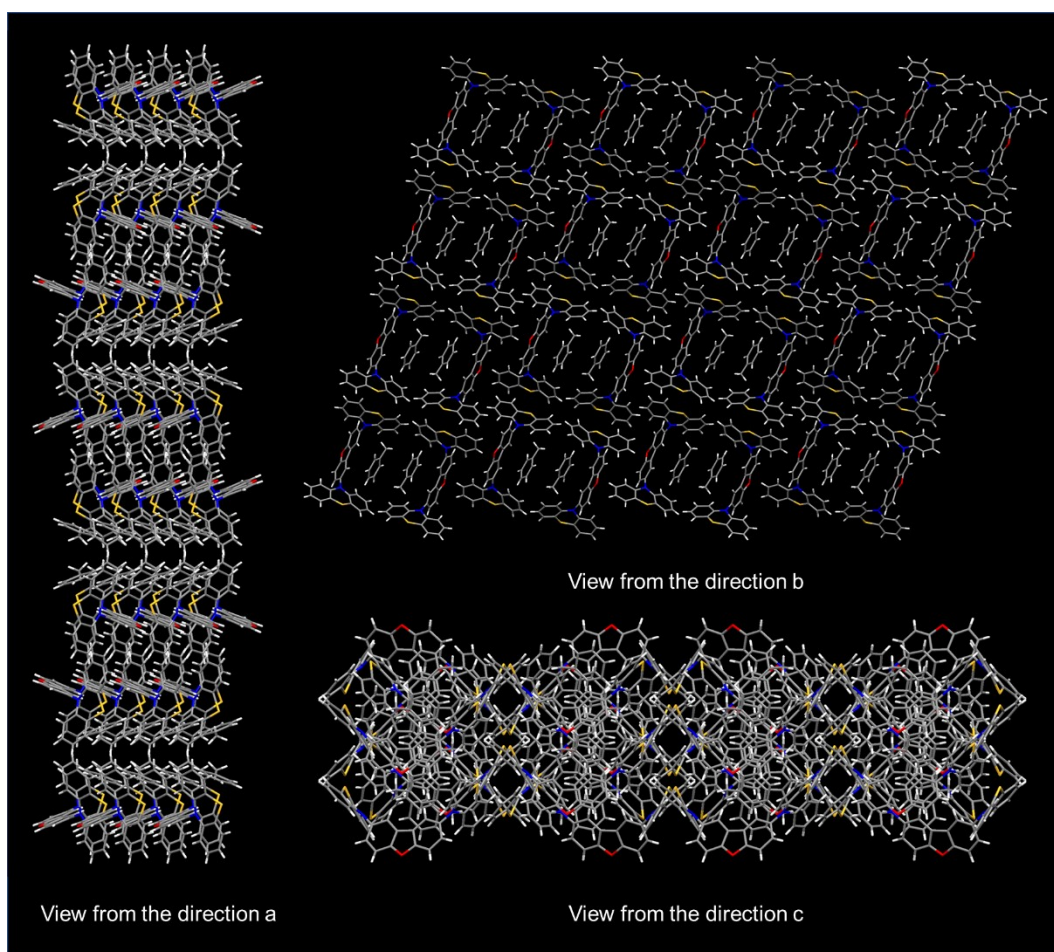
Figure S33. Molecular packing of **PBO-3** crystal observed from a, b, and c directions, respectively. Single crystal **PBO-3** is obtained by slowly volatilizing toluene solution.

(a) 10.69 Å, 10.12 Å

C-H···π (3.10 Å – 3.93 Å)

(b)

C-H···π (3.15 Å – 3.79 Å)
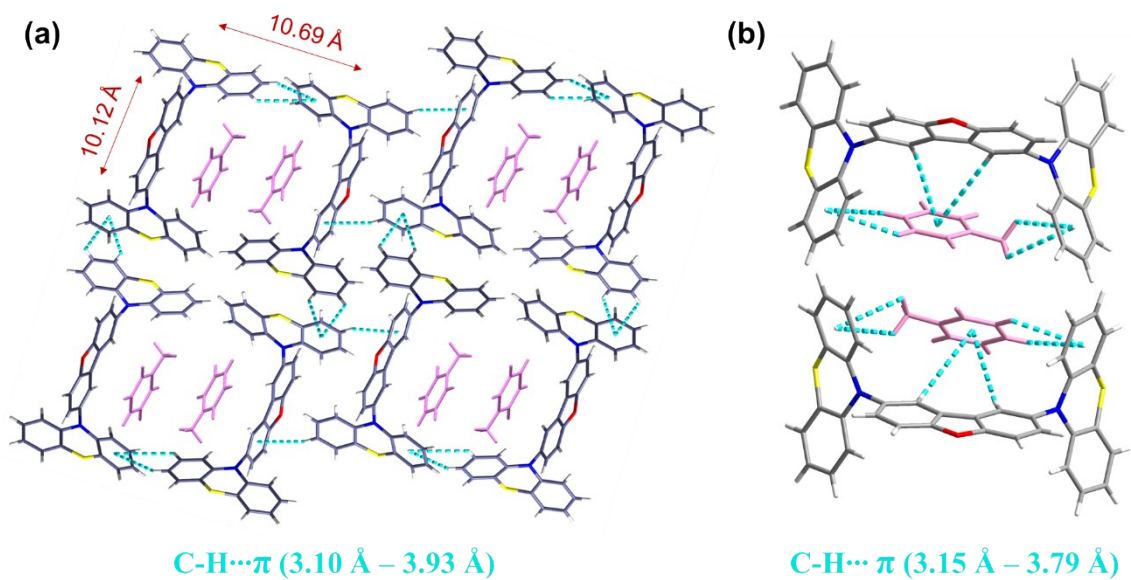
Figure S34. Pore size analyses and molecular interactions of **PBO-3**.
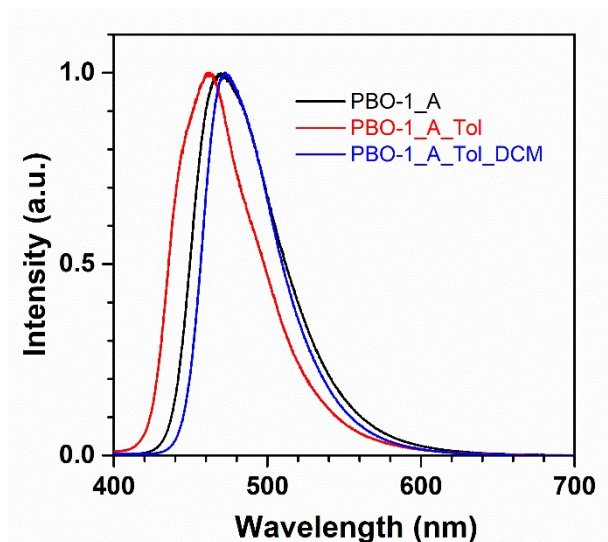
Figure S35. Photoluminescence (PL) spectra of **PBO-1_A** (**PBO-1** after high temperature activation), **PBO-1_A_Tol** (**PBO-1_A** is exposed to toluene vapour), **PBO-1_A_Tol_DCM** (**PBO-1_A_Tol** is exposed to dichloromethane vapour)**.**
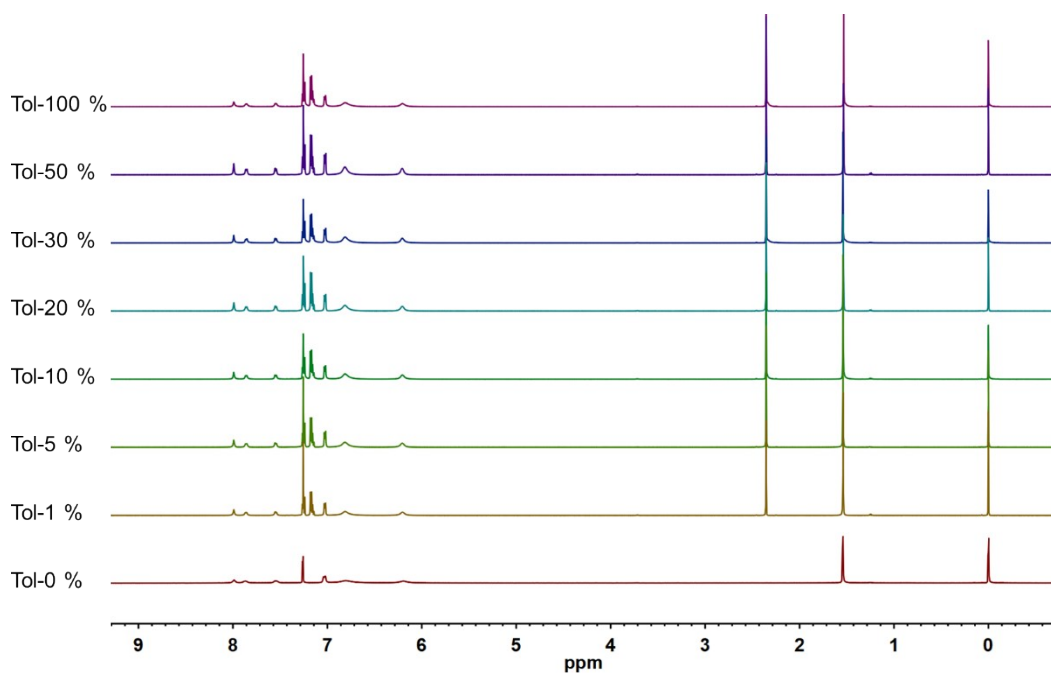
Figure S36. ^{1}H NMR (600 MHz, CDCl$_3$) spectra of **PBO-1_A** exposed to different toluene/water mixtures.
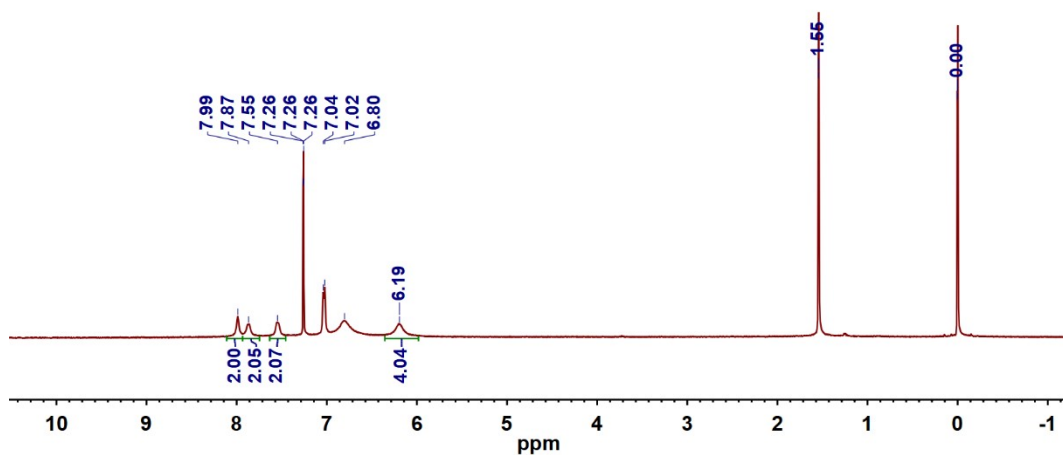
Figure S37. ^{1}H NMR (600 MHz, CDCl$_3$) spectrum of **PBO-1_A**
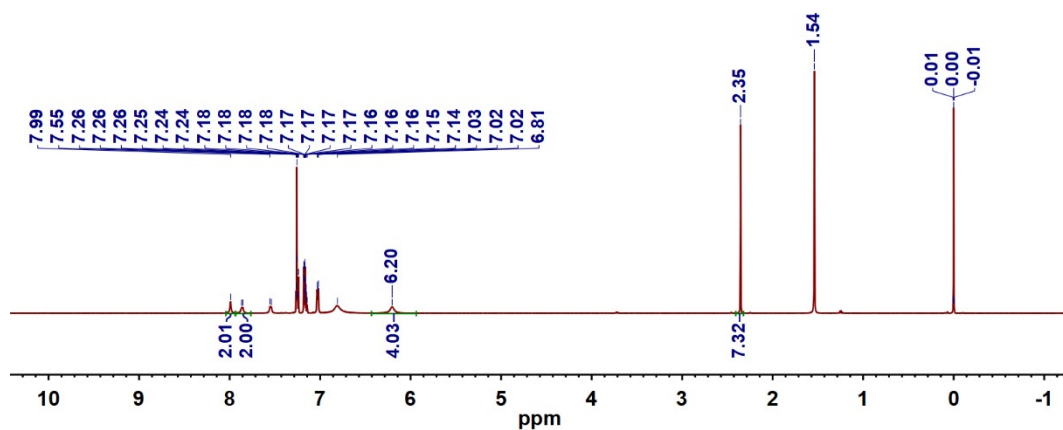
Figure S38. ^{1}H NMR (600 MHz, CDCl$_3$) spectrum of **PBO-1_A-Tol-1%**
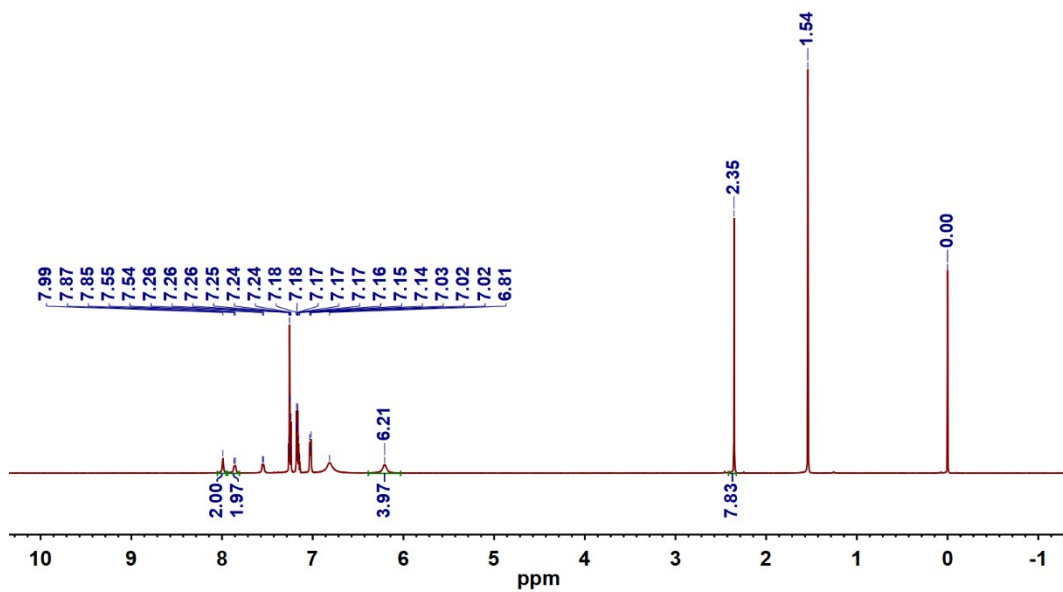
Figure S39. ^{1}H NMR (600 MHz, CDCl$_3$) spectrum of **PBO-1_A-Tol-5%**
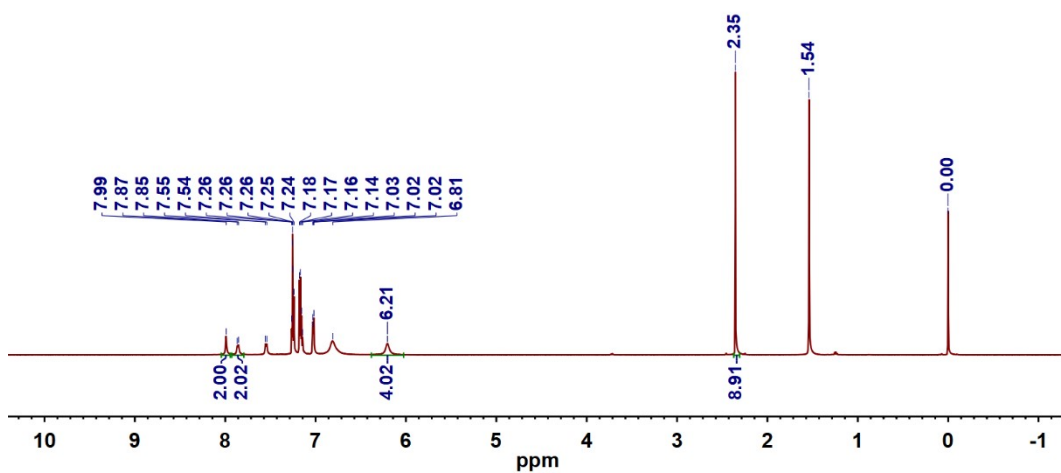
Figure S40. ^{1}H NMR (600 MHz, CDCl$_3$) spectrum of **PBO-1_A-Tol-10%**
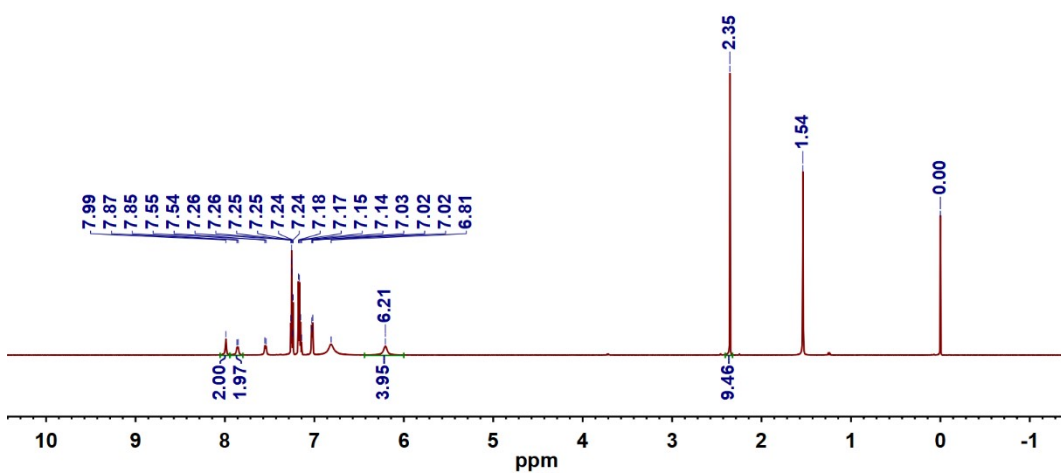
Figure S41. ^{1}H NMR (600 MHz, CDCl$_3$) spectrum of **PBO-1_A-Tol-20%**
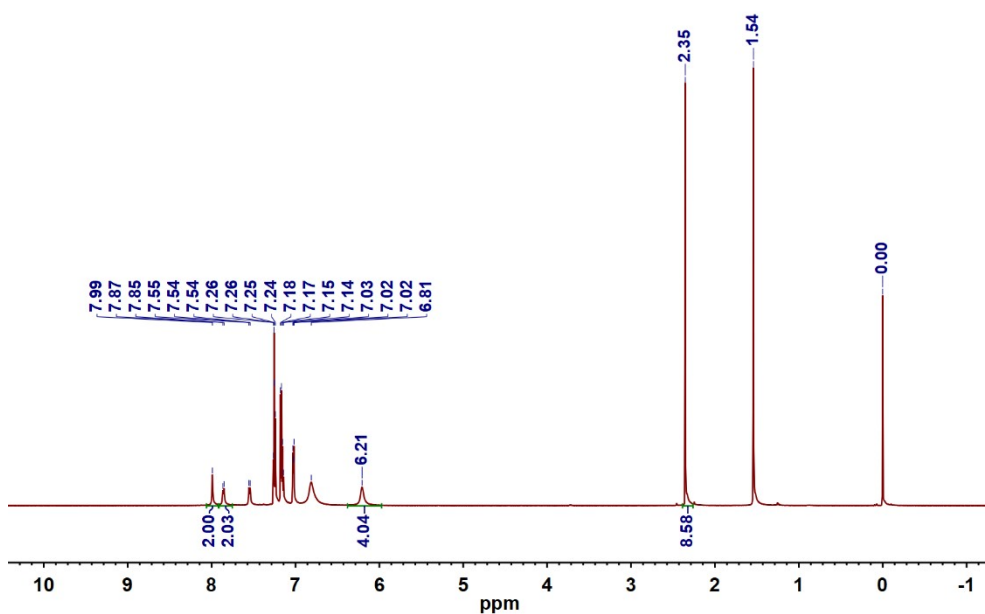
Figure S42. ^{1}H NMR (600 MHz, CDCl$_3$) spectrum of **PBO-1_A-Tol-30%**

33
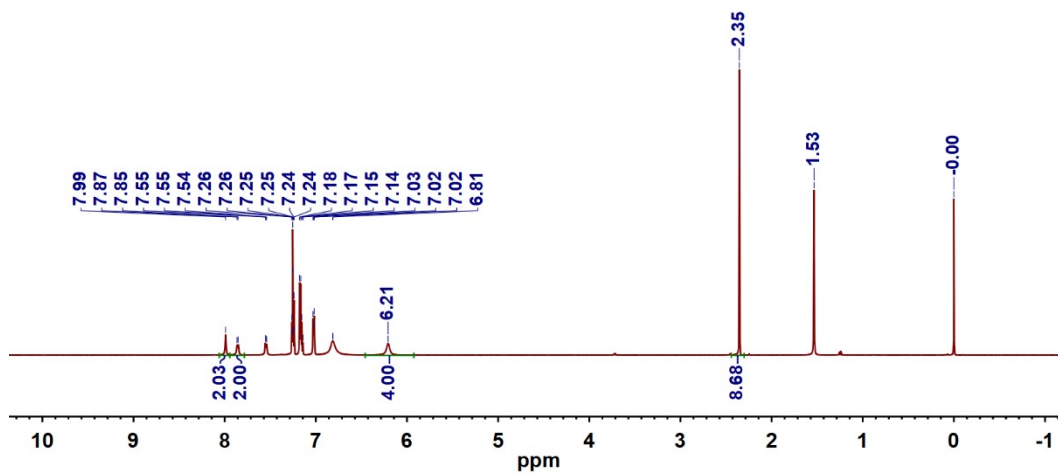
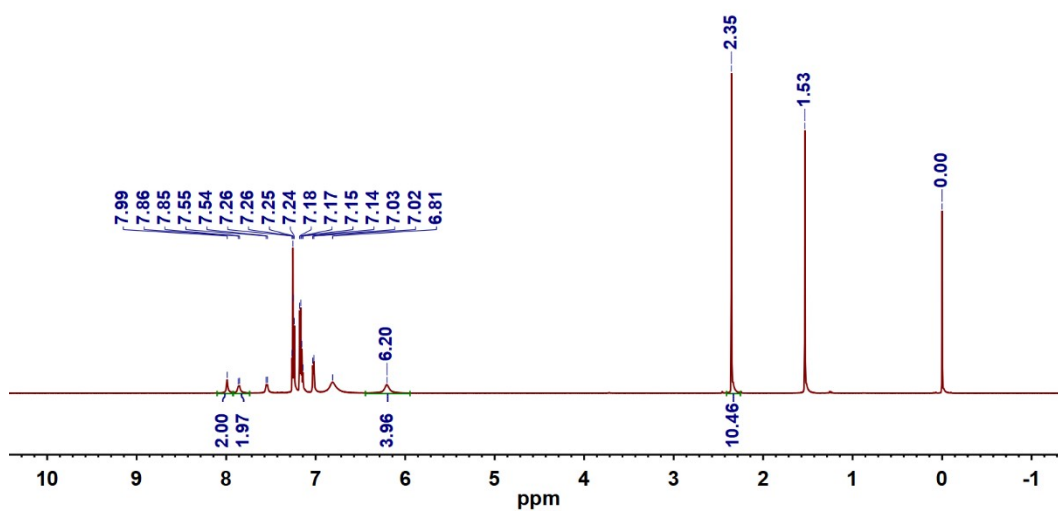**Figure S43.** ^{1}H NMR (600 MHz, CDCl$_3$) spectrum of **PBO-1_A-Tol-50%**

Figure S44. ^{1}H NMR (600 MHz, CDCl$_3$) spectrum of **PBO-1_A-Tol-100%**

Table S4. Toluene vapor adsorption data recorded at 298 K for **PBO-1_A**.

Volume fraction of toluene (%)	Toluene absorption (mmol g^{-1})
0	0
1	4.34
5	4.64
10	5.28
20	5.61
30	5.09
50	5.15
100	6.20
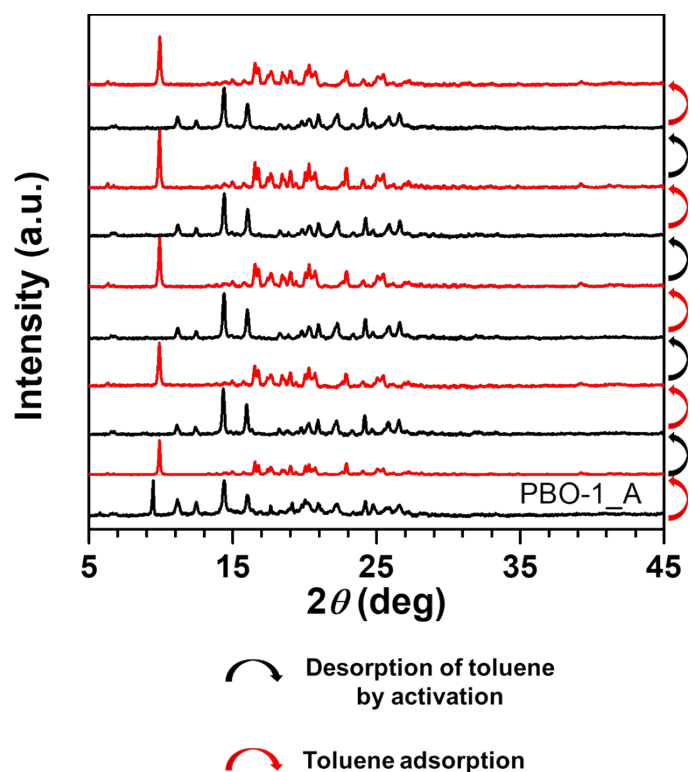
Figure S45. PXRD patterns of **PBO-1_A** of toluene adsorption and desorption process by thermal activation treatment.
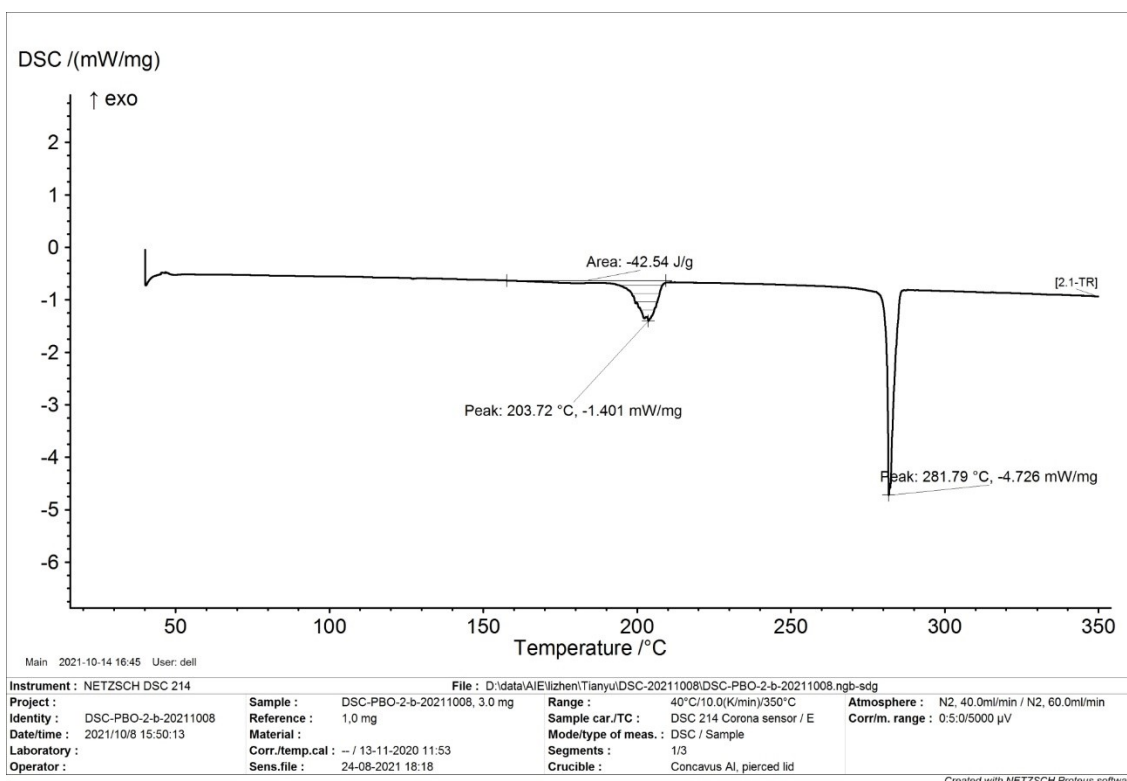

Figure S46. a) The DSC curve and analysis results for the crystal **PBO-2**. Combined with crystal data, the heat required for each molar dichloromethane to escape from crystals is 51485 Joules.
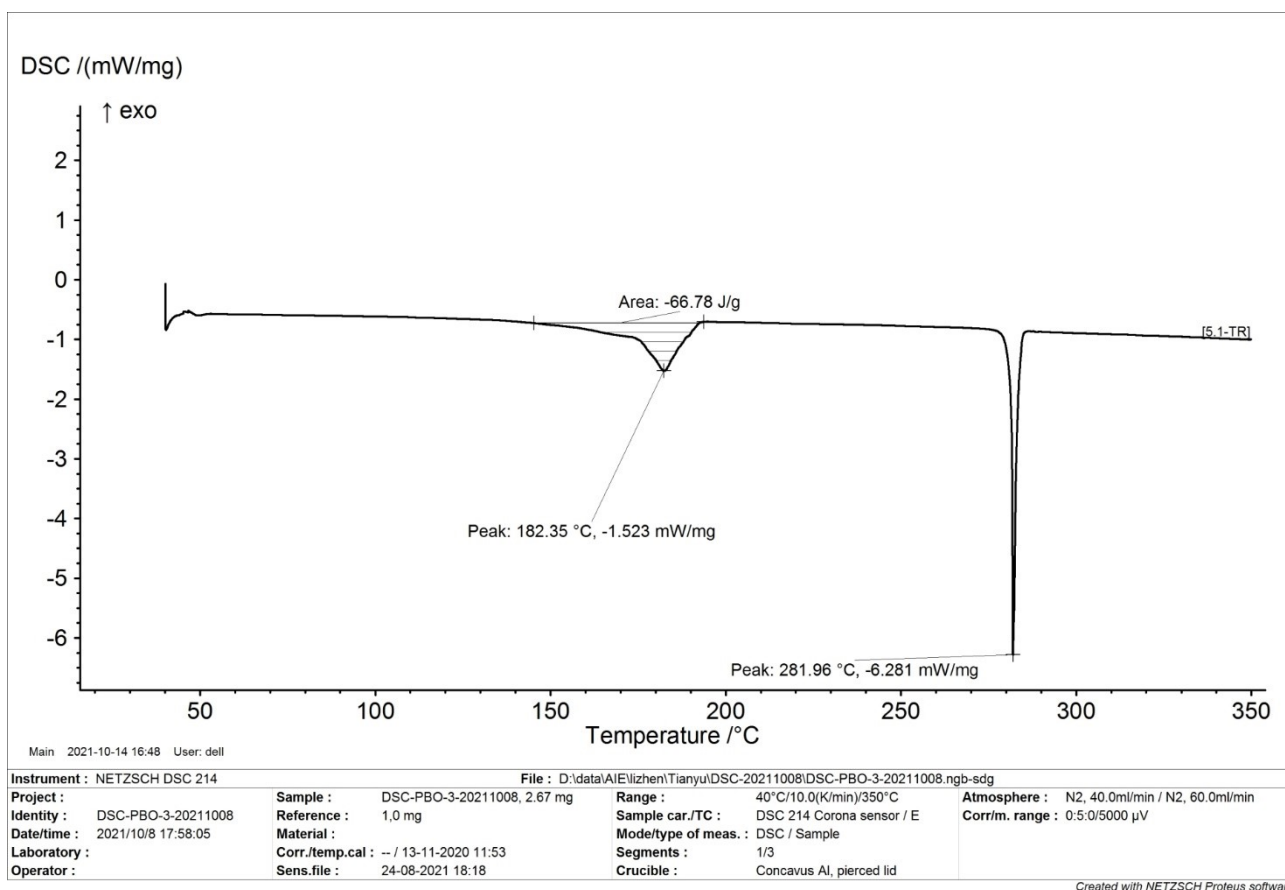
Figure S47. a) The DSC curve and analysis results for the crystal **PBO-3**. Combined with crystal data, the heat required for each molar dichloromethane to escape from crystals is 43728 Joules.

The specific calculation method is as follows. According to the crystal data of PBO-2, the crystal mass containing one mole of dichloromethane molecules is 1210.28 grams; and DSC curve analysis of PBO-2 displays the result that 42.54 Joule heat is required when the dichloromethane is completely escaping from the one-gram crystal PBO-2. Then, the heat required for each molar dichloromethane completely escaping from the crystal PBO-2 should be 1210.28 g/mol * 42.54 J/g = 51485 J/mol. Similarly, the heat required for each molar toluene completely escaping from the crystal PBO-3 should be 654.81 g/mol * 66.78 J/g = 43728 J/mol.
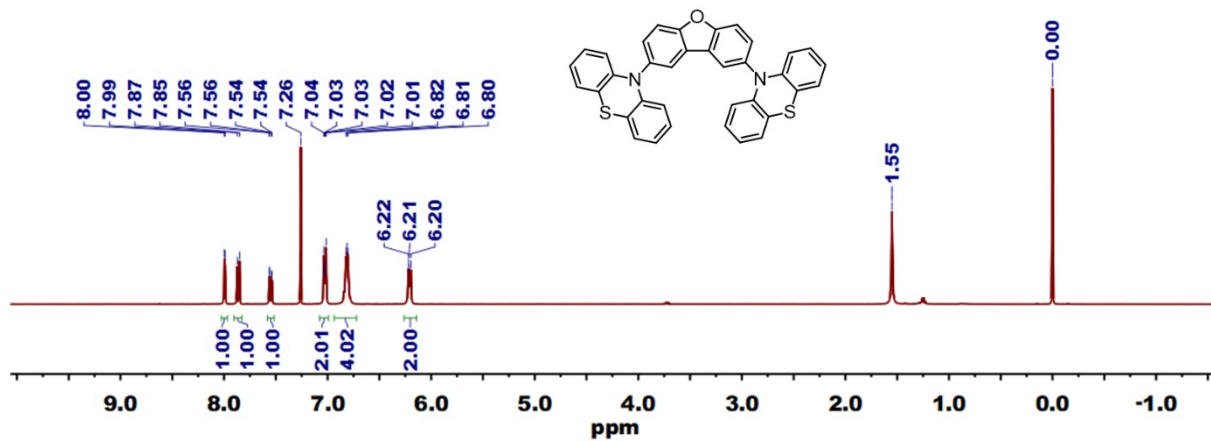
6. NMR, HRMS Spectra of PBO and PBS (Figures S48-S53)

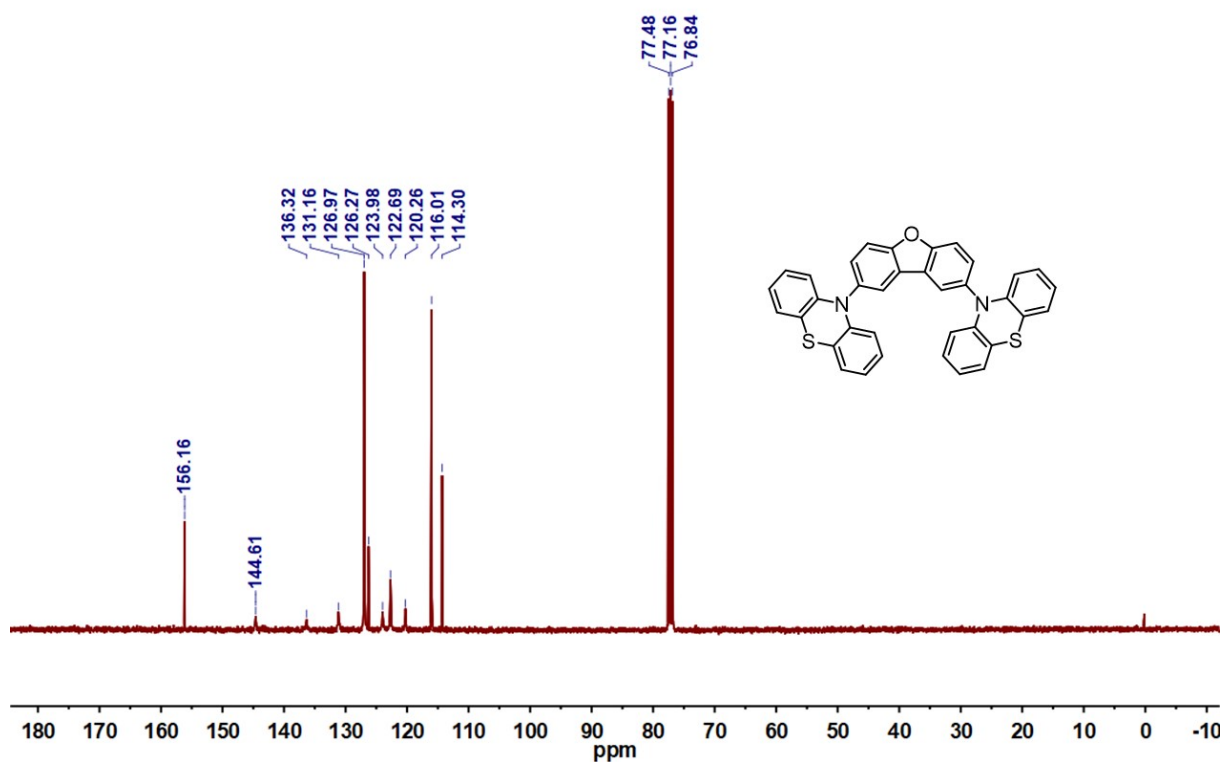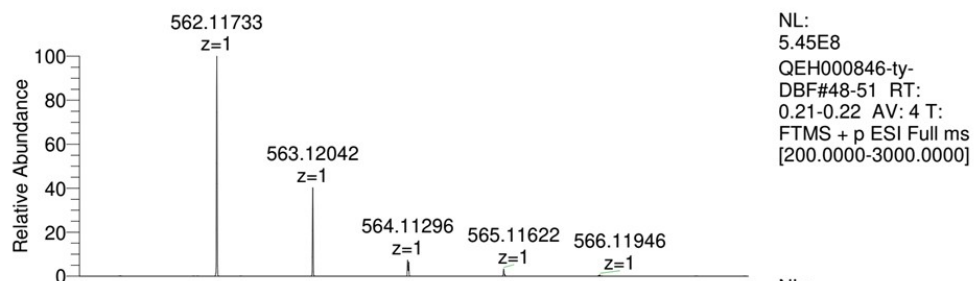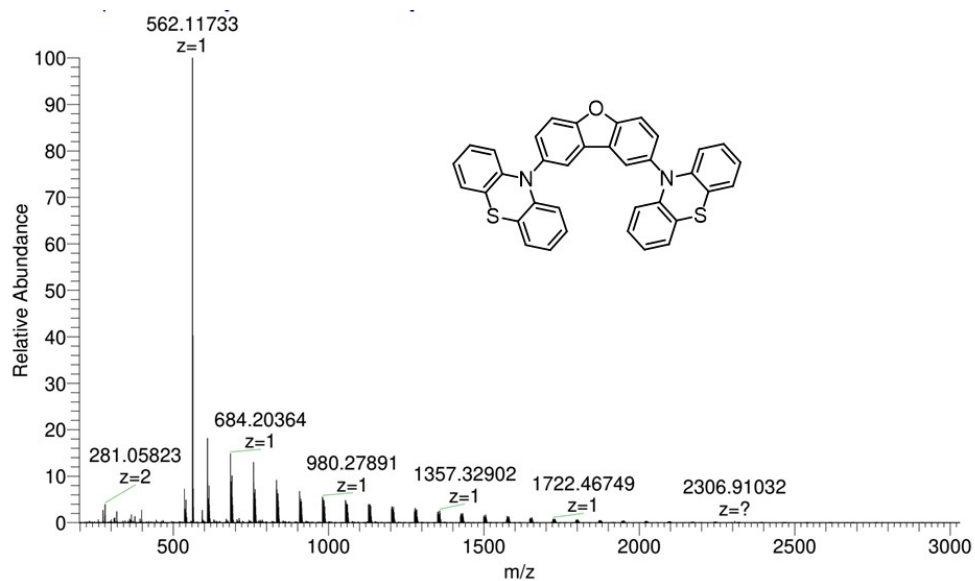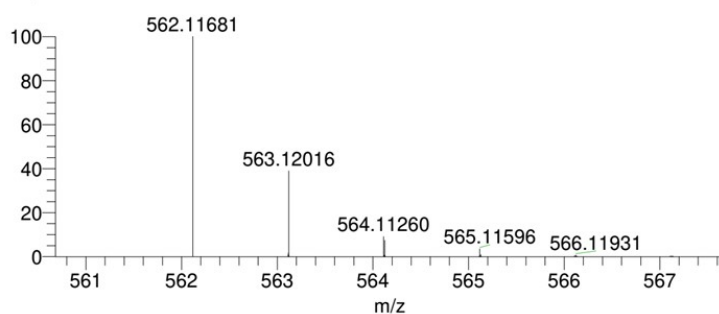**Figure S48.** ^{1}H NMR (400 MHz, CDCl3) spectrum of **PBO**.

Figure S49 ^{13}C NMR (100 MHz, CDCl3) spectrum of **PBO**.
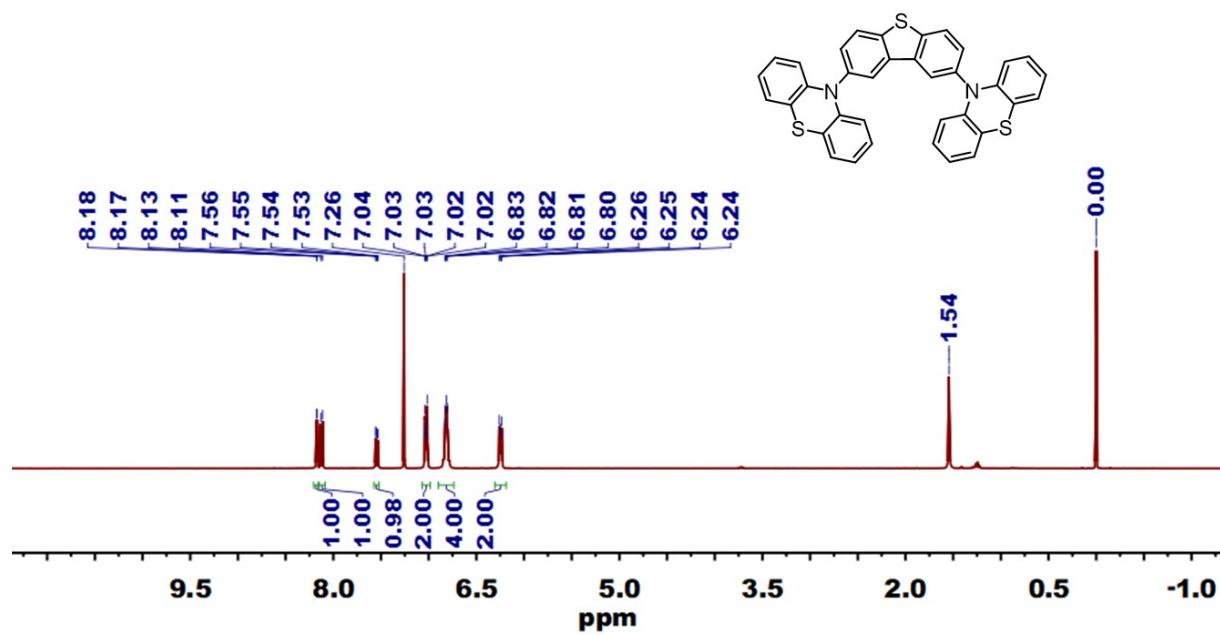
Figure S50. HRMS-ESI spectrum of **PBO**.
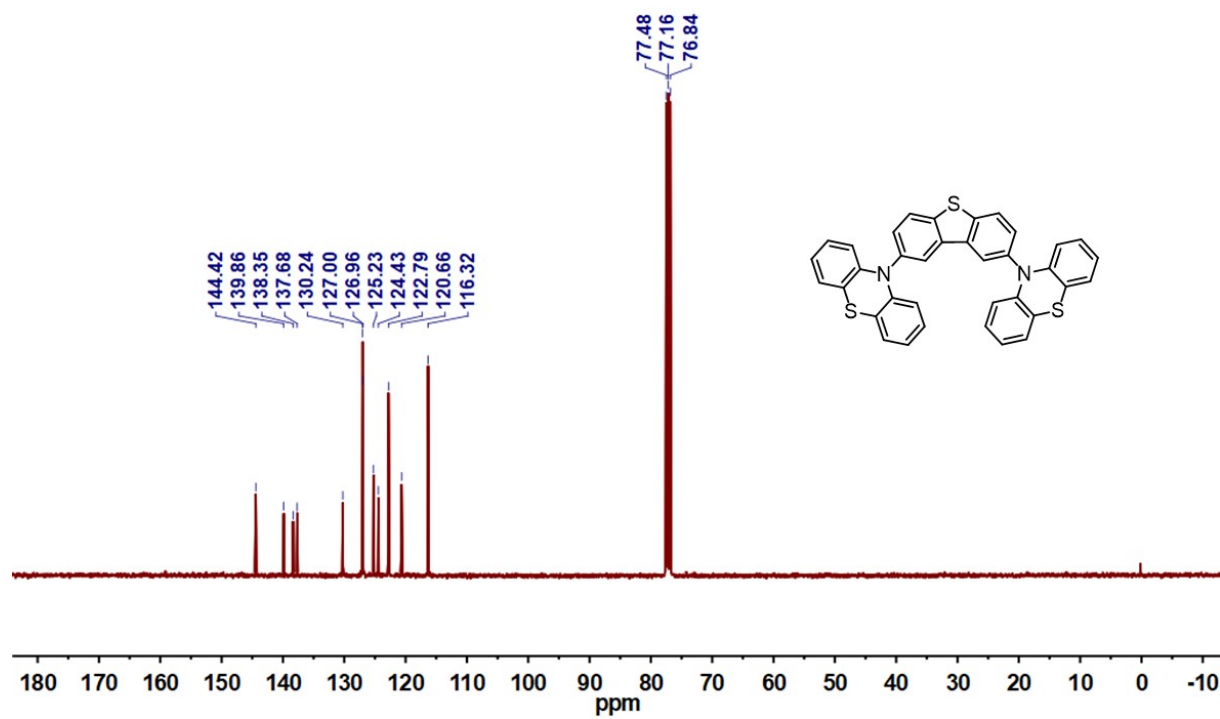
Figure S51. ^{1}H NMR (400 MHz, CDCl$_3$) spectrum of **PBS**.

Figure S52. ^{13}C NMR (100 MHz, CDCl$_3$) spectrum of **PBS**.
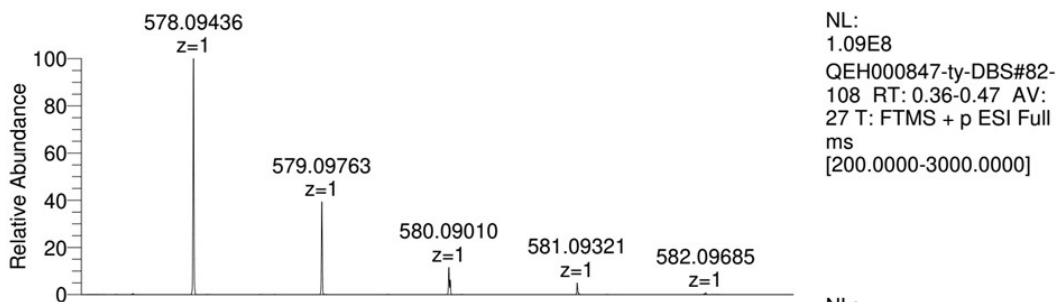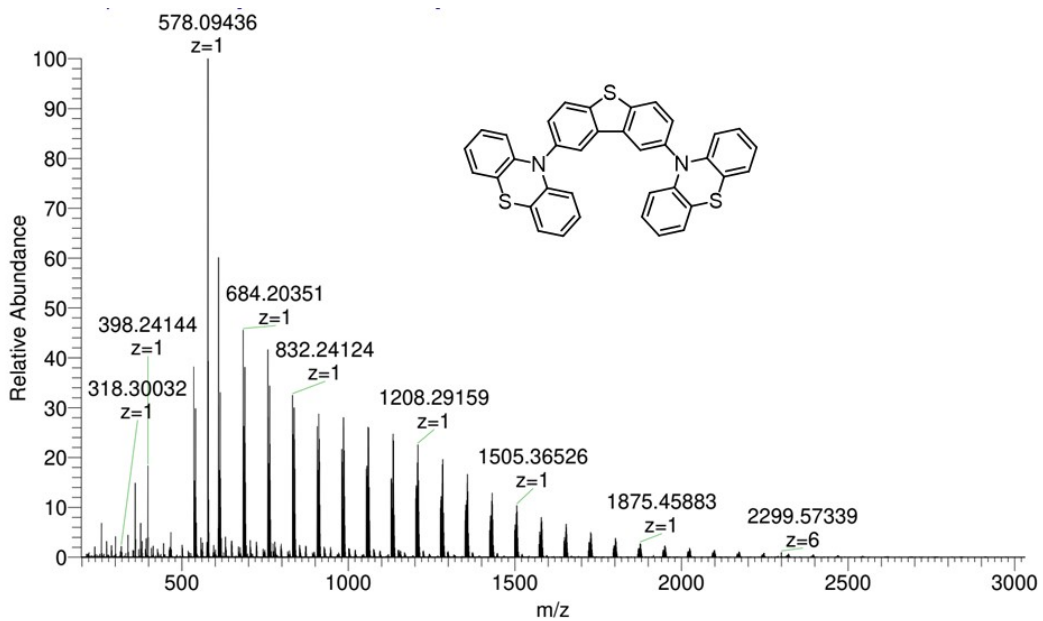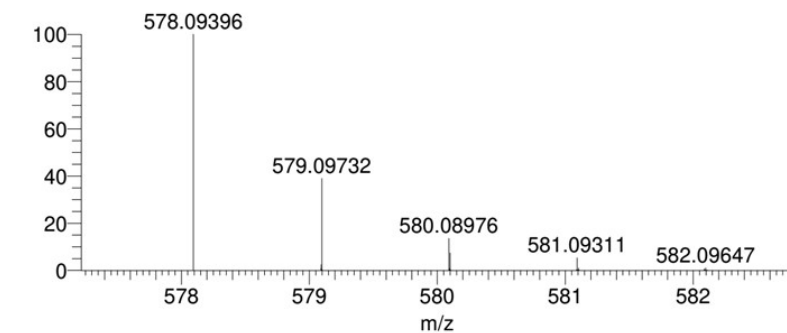
Figure S53. HRMS-ESI spectrum of **PBS**.

7. References

S1. Zhang, X. et al. Selective ethane/ethylene separation in a robust microporous hydrogen-bonded organic framework. *J. Am. Chem. Soc.* **142**, 633−640 (2020).

S2. Zhou, Y. et al. Self-assembly of homochiral porous supramolecular organic frameworks with significant CO_2 capture and CO_2/N_2 selectivity. *Cryst. Growth Des.* **17**, 6653–6659 (2017).

S3. Wahl, H., Haynes, D.A. & Roex T. Guest exchange in a robust hydrogen-bonded organic framework: single-crystal to single-crystal exchange and kinetic studies. *Cryst. Growth Des.* **17**, 4377–4383 (2017).

S4. Sanchez-Sala, M., Vallcorba, O., Domingo, C. & Aylloń, J.A. A flexible hydrogen bonded organic framework that reversibly adsorbs acetic acid: γ trimesic acid. *Cryst. Growth Des.* **18**, 6621−6626 (2018).

S5. Hisaki, I. et al. Acid responsive hydrogen-bonded organic frameworks. *J. Am. Chem. Soc.* **141**, 2111−2121 (2019).

S6. Chen, T.H. et al. Thermally robust and porous noncovalent organic framework with high affinity for fluorocarbons and CFCs. *Nat. Commun.* **5**, 5131 (2014).

S7. Maly, K.E., Gagnon, E., Maris, T. & Wuest, J.D. Engineering hydrogen-bonded molecular crystals built from derivatives of hexaphenylbenzene and related compounds. *J. Am. Chem. Soc.* **129**, 4306–4322 (2007).

S8. Maly, K.E., Buck, W. & Dawe, L.N. Open network structures from 2D hydrogen bonded networks: diaminotriazyl tetraoxapentacenes. *CrystEngComm.* **19**, 6401-6405 (2017).

S9. Li, P. et al. A homochiral microporous hydrogen-bonded organic framework for highly enantioselective separation of secondary alcohols. *J. Am. Chem. Soc.* **136**, 547-549 (2014).

S10. He, Y.B., Xiang, S.C. & Chen, B.L. A microporous hydrogen-bonded organic framework for highly selective C_2H_2/C_2H_4 separation at ambient temperature. *J. Am. Chem. Soc.* **133**, 14570–14573 (2011).

S11. Luo, X.Z. et al. A microporous hydrogen-bonded organic framework: exceptional stability and highly selective adsorption of gas and liquid. *J. Am. Chem. Soc.* **135**, 11684–11687 (2013).

S12. Morshedi, M., Thomas, M., Tarzia, A., Doonan, C. J. & White, N. G. Supramolecular anion recognition in water: synthesis of hydrogen-bonded supramolecular frameworks. *Chem. Sci.* **8**, 3019–3025 (2017).

S13. Chaumont, C., Mobian, P., Kyritsakas, N., & Henry, M. Synthesis, topology and energy analysis of crystalline resorcinol-based oligophenylene molecules with various symmetries. *CrystEngComm.* **15**, 6845–6862 (2013).

S14. Li, P. et al. Solvent dependent structures of hydrogen-bonded organic frameworks of 2,6-Diaminopurine. *Cryst. Growth Des.* **14**, 3634–3638 (2014).

S15. Liu, L. et al. Supramolecular network of triaminotriptycene and its water cluster guest: synthesis, structure, and characterization of $[(tatp)_4 \cdot 17H_2O]_n$. *Cryst. Growth Des.* **18**, 1629–1635 (2018).

S16. Makowski, S. J., Köstler, P. & Schnick, W. Formation of a hydrogen-bonded heptazine framework by self-assembly of melem into a hexagonal channel structure. *Chem. Eur. J.* **18**, 3248–3257 (2012).

S17. Yamagishi, H. et al. Self-assembly of lattices with high structural complexity from a geometrically simple molecule. *Science* **361**, 1242-1246 (2018).